International Journal of Geo-Information

MDPI

Article

Identifying Climate and Anthropogenic Risks Along the Beijing–Hangzhou Grand Canal Using GIS-Based Spatiotemporal Analysis

Junyi Shi [1,2], Lijun Yu [1,2,3,*], Ze Liu [4], Hui Wang [5] and Yueping Nie [1,2]

[1] Aerospace Information Research Institute, Chinese Academy of Sciences, Beijing 100101, China
[2] University of Chinese Academy of Sciences, Beijing 100049, China
[3] International Centre on Space Technologies for Natural and Cultural Heritage Under the Auspices of UNESCO, Beijing 100094, China
[4] Research Centre for Spatial Planning, Ministry of Natural Resources, Beijing 100034, China
[5] Institute of Scientific and Technological Archaeology, Fudan University, Shanghai 200433, China
* Correspondence: yulj@aircas.ac.cn

Abstract

Linear heritage corridors are increasingly exposed to spatially heterogeneous pressures from climate change and human activities, yet integrated geospatial frameworks for corridor-scale risk identification remain limited. Taking the Beijing–Hangzhou Grand Canal as a representative linear World Heritage corridor, this study developed a GIS-based spatiotemporal assessment framework to quantify natural risk, anthropogenic pressure, and their coupled patterns during 1995–2024. Approximately 350 canal segments were constructed as comparable assessment units and linked with 49 heritage sites and 18 World Heritage canal sections through a multi-scale spatial framework integrating canal sections, buffer zones, and heritage sites. Natural risk was characterized using extreme temperature, precipitation, and drought indices, while anthropogenic pressure was represented by nighttime lights, population density, impervious surface, and road density. The results reveal a clear north–south gradient in integrated natural risk, with higher values concentrated in the southern canal sections. Among the three natural-risk modules, temperature, precipitation, and drought contributed weights of 0.594, 0.242, and 0.164, respectively, indicating the dominant role of heat-related processes. The first two principal components of anthropogenic pressure explained 80.8% of the total variance. Four dominant coupling types were identified, among which the dual high-pressure type was concentrated mainly in the southern canal and marked the most critical areas of compound risk. This study provides a geospatial approach for hotspot detection and spatial decision support for the conservation of large linear heritage systems.

Keywords: linear heritage corridor; spatiotemporal analysis; climate risk; anthropogenic pressure; coupled risk patterns

Check for updates

Academic Editors: Wolfgang Kainz, Cheng Li, Fei Zhang, Mou Leong Tan and Kwok Pan Chun

Received: 16 April 2026
Revised: 15 May 2026
Accepted: 18 May 2026
Published: 22 May 2026

Copyright: © 2026 by the authors. Published by MDPI on behalf of the International Society for Photogrammetry and Remote Sensing. Licensee MDPI, Basel, Switzerland. This article is an open access article distributed under the terms and conditions of the Creative Commons Attribution (CC BY) license.

1. Introduction

The Beijing–Hangzhou Grand Canal, one of the longest and best-preserved artificial waterways in the world, is a representative linear cultural heritage system [1]. Extending across northern and southern China, it links diverse regional natural and cultural landscapes and embodies the ingenuity of ancient hydraulic engineering as well as the historical and cultural values shaped by settlement development along its corridor [2]. Like many cultural heritage

systems, however, the Grand Canal and its associated heritage elements are increasingly exposed to rapid environmental change and intensified human disturbance [3–5]. Under the dual pressures of climate change and accelerating urbanization [6,7], cultural heritage conservation has become an important component of sustainable development and cultural security, as explicitly recognized in Sustainable Development Goal (SDG) 11.4, which calls for strengthening efforts to protect and safeguard the world's cultural and natural heritage [8].

For a cross-regional and long-distance linear heritage corridor such as the Beijing–Hangzhou Grand Canal, effective conservation requires continuous monitoring and assessment of key risk drivers, particularly extreme climate events and anthropogenic pressures, because these jointly affect the stability of the heritage environment and its long-term degradation processes [9–11]. In recent years, the Grand Canal and its associated heritage elements have been increasingly exposed to climate-related risks, including extreme heat, intense precipitation, and drought, as well as to urban development pressures such as population concentration, impervious surface expansion, and infrastructure construction [12,13]. These pressures have generated pronounced spatiotemporal heterogeneity in conservation risk among different canal sections. Establishing an integrated risk monitoring and assessment framework under the combined pressures of climate change and human activities is therefore essential for identifying high-risk sections, optimizing conservation priorities, and enhancing sustainable management capacity [9,12–15].

Recent studies have provided an important methodological basis for quantitative heritage risk assessment. On the one hand, extreme climate indices, disaster statistics, and scenario-based approaches have been widely used to characterize natural risk, as extreme climate events and natural hazards can destabilize heritage environments and accelerate material deterioration through processes such as extreme heat, intense precipitation, drought, and flooding [9–11,14–16]. For example, Sardella et al. [17] developed risk maps for cultural heritage conservation in Europe and the Mediterranean based on ETCCDI-defined extreme climate indices and supported decision-making through a Web GIS platform, while Kim et al. [18] further demonstrated the feasibility of ETCCDI-based composite risk characterization using correlation screening, variance inflation factor (VIF) testing, and entropy-based weighting. On the other hand, the rapid development of remote sensing and geospatial data has enabled indicators such as population density, nighttime lights, impervious surfaces, and land-use change to be widely used for characterizing anthropogenic pressure, urbanization-related disturbance, and associated environmental effects [13,19–21]. For instance, Moise et al. [22] used multi-temporal remote sensing data to analyze land-use change and built-up expansion around the historic urban landscape of Alba Iulia, showing that built-environment change can serve as an important proxy for human disturbance in heritage surroundings. Nighttime light data have likewise been increasingly applied to capture urbanization processes and development intensity, providing an effective supplement for identifying persistent anthropogenic pressure around heritage corridors [23]. Building on these advances, some studies have further integrated hazard, exposure, and vulnerability within unified frameworks to support spatial risk classification and the identification of priority areas [14–16,24].

Overall, existing studies have demonstrated the applicability of methods for both natural risk characterization and the quantification of human activities, providing an important foundation for the quantitative identification of cultural heritage risk. However, extreme climate risk and urbanization-related disturbance are still often examined separately, with relatively few studies incorporating both within a unified quantitative framework. This limits the ability to identify risk patterns and dominant driving types under the joint effects of these dual pressures. In addition, most previous studies have focused on individual heritage sites, historic urban areas, or localized regional cases, whereas corridor-wide

assessments of risk evolution remain insufficient for cross-regional, long-distance linear heritage systems. Research outputs also tend to remain at the level of areal risk maps or localized site identification, with limited translation into management-oriented inventories of high-risk sections and priority heritage sites. It is therefore necessary to integrate extreme climate indicators and proxies of human activity within a unified spatial framework and to develop a comprehensive dual-pressure assessment approach for linear cultural heritage corridors.

To address these limitations, this study focuses on the Beijing–Hangzhou Grand Canal and its associated heritage sites and develops a GIS-based multi-scale integrated risk assessment framework under the dual pressures of climate change and human activities. The framework is designed to characterize risk evolution during 1995–2024 and to identify canal sections exposed to compound high risk within a unified geospatial analytical structure. Unlike previous studies that have largely focused on localized sites, single risk types, or static spatial patterns, this study integrates natural risk and anthropogenic pressure within a unified spatial framework to reveal their coupled spatiotemporal characteristics across both the full corridor and a long-term temporal sequence. The main advances of this study are threefold:

(1) At the spatial scale, it establishes comparable segment-based assessment units by integrating heritage sites, canal reaches, and surrounding environments within a unified multi-scale framework, thereby enabling continuous risk identification and cross-sectional comparison along the entire canal.

(2) At the temporal scale, it uses multi-source time-series data from 1995 to 2024 to examine whether risk is intensifying, weakening, or fluctuating, thus providing a more comprehensive understanding of corridor-scale risk evolution.

(3) In terms of integrated analysis and geospatial application, it combines climate-related risk and anthropogenic pressure to identify dominant risk sources, coupling types, high-risk canal sections, and priority heritage sites, thereby supporting hotspot detection, spatial decision support, and differentiated management for large linear heritage systems.

2. Data and Methods

2.1. Study Area

The Beijing–Hangzhou Grand Canal is one of the longest and largest ancient canal systems in the world and one of the oldest surviving artificial waterways (Figure 1). Extending from Hangzhou in the south to Beijing in the north, it passes through the present-day provinces of Zhejiang, Jiangsu, Shandong, and Hebei, as well as the municipalities of Tianjin and Beijing, connecting the Hai River, Yellow River, Huai River, Yangtze River, and Qiantang River systems. With a total length of approximately 1794 km, it forms a cross-basin and cross-regional inland waterway corridor [25,26]. As a representative linear cultural heritage corridor, the Grand Canal contains diverse heritage elements distributed along its route, including canal bodies, hydraulic remains, historic towns, and associated cultural landscapes. Its core heritage components include 49 World Heritage sites and 18 World Heritage canal sections, which together preserve the historical information of canal transport, grain tribute administration, and settlement development along the corridor [1]. In recent years, under the combined influences of climate change and rapid urbanization, the hydrological processes, riparian environments, and heritage settings along the canal have been subjected to increasingly complex natural and anthropogenic pressures, making it a representative study area for heritage risk assessment.

In this study, corridor-based analytical units were constructed along the canal centerline. To capture the direct influence of the near-channel environment on heritage sites while maintaining a spatial extent suitable for corridor-scale comparison, a 2 km buffer was

defined as the core study area. This distance is consistent with previous GIS-based studies on cultural routes and heritage landscapes, in which 2 km buffers were used to delineate near-route heritage environments and to analyze surrounding land-use and landscape change [27–29]. Within this range, the selected extreme climate and drought indicators were spatially aggregated for each year, and a human activity intensity index was further derived to construct annual sequences of natural risk and anthropogenic pressure at the canal-segment scale. In the exposure assessment stage, integrated segment-level risk values were spatially assigned to the corresponding heritage sites, thereby linking corridor-scale risk patterns with site-level exposure.

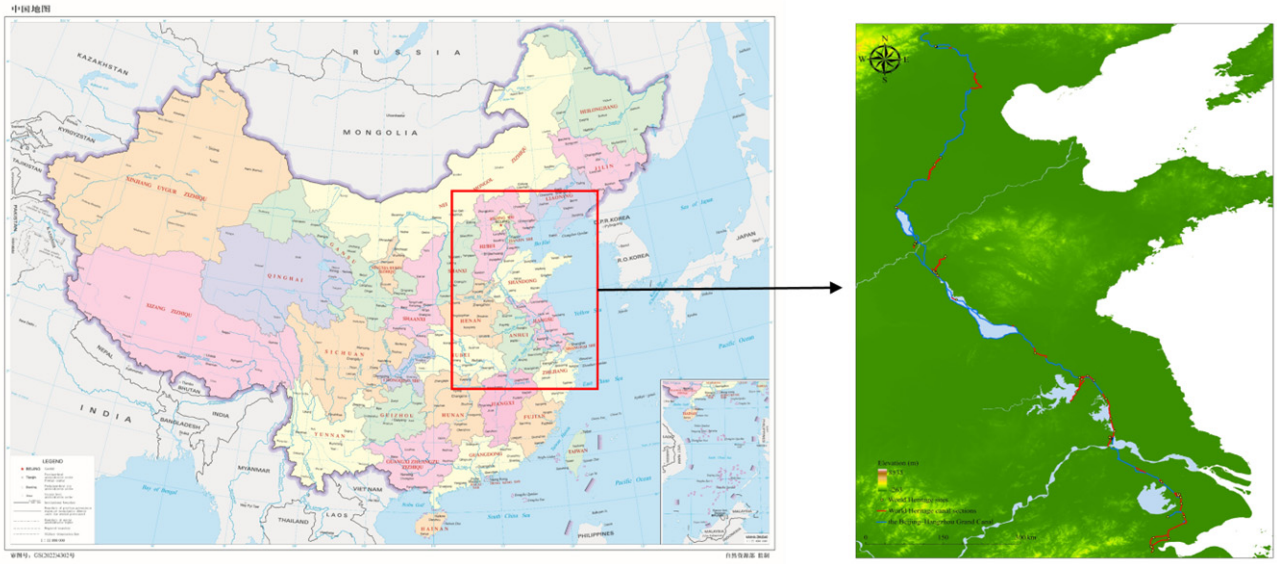


Figure 1. Overview of the study area of the Beijing–Hangzhou Grand Canal.

2.2. Data Collection and Preprocessing

2.2.1. Precipitation and Temperature Data

Climate variables used in this study were obtained from the China Meteorological Forcing Dataset (ChinaMet) released by the National Meteorological Science Data Center (NCDC; https://www.ncdc.ac.cn, accessed on 15 December 2025) [30,31]. This dataset was developed by integrating observations from more than 2000 meteorological stations with multi-source remote sensing products and reanalysis data. It provides long-term coverage (1980–2024) and high spatial resolution (approximately 1 km, corresponding to 0.01°), making it well-suited to the identification of extreme climate events and regional-scale risk assessment. ChinaMet includes multiple meteorological variables, such as precipitation (prec), 2 m mean air temperature (tmpmean), maximum air temperature (tmpmax), and minimum air temperature (tmpmin), and provides annual, monthly, and daily products at spatial resolutions of 0.1° and 0.01°.

In terms of data sources, the precipitation product (prec) integrates station observations with multiple satellite-based precipitation datasets, including IMERG, CMORPH, and SM2RAIN-ASCAT, as well as ERA5-Land reanalysis data. The temperature-related variables (tmpmean, tmpmax, and tmpmin) are derived from station observations combined with multi-source information, including AVHRR and MODIS land surface temperature products (MOD11A1 and MYD11A1) and ERA5-Land.

Based on these daily precipitation and temperature data, this study calculated a series of ETCCDI (Expert Team on Climate Change Detection and Indices) extreme climate indices to characterize extreme temperature and precipitation conditions. These included heat-related indicators, such as TXx, SU25, TR20, and WSDI, as well as heavy precipitation

and persistent wetness indicators, such as Rx1day, R20, and CWD. These indices were used to capture the spatial variability and interannual trends of extreme events along the Beijing–Hangzhou Grand Canal. In addition, to characterize regional drought processes and water deficit conditions, the Standardized Precipitation Evapotranspiration Index (SPEI) was calculated based on precipitation series and evapotranspiration data, and key statistics, such as the annual minimum value, were extracted as indicators of drought risk. Together, these variables formed a multidimensional natural risk indicator system covering heat, flooding, and drought, providing the basis for subsequent integrated risk assessment and the identification of dominant risk types.

2.2.2. Human Activity Data

To characterize the intensity of human activities and their potential disturbance pressures along the Beijing–Hangzhou Grand Canal, this study constructed a human activity indicator system using multi-source data on land use, nighttime lights, population density, and transportation infrastructure. The details are as follows.

(1) Land use

Land-use data were derived from the annual 30 m China Land Cover Dataset (CLCD, 1985–2025) published by Yang and Huang [32]. Based on Landsat imagery, this dataset provides annual land-cover classification rasters at 30 m resolution and can be used to characterize long-term changes in land-cover patterns and built-up land expansion during the study period. The data were obtained from Zenodo (https://zenodo.org/records/5816591, accessed on 15 December 2025). Based on this dataset, impervious surface information, particularly built-up land, was extracted as an indicator of human activity intensity. The proportion of impervious surfaces within each 1 km grid cell was then calculated to construct the impervious surface fraction indicator, which represents the hardening of the land surface driven by urbanization.

(2) Nighttime lights

Nighttime light data were obtained from the annual Extended VIIRS-like Artificial Nighttime Light (EVAL) dataset (1986–2024) [33]. This product maintains good temporal consistency over a long time series and has been widely used to characterize spatial differences in population activity, economic vitality, and human disturbance intensity [13,33]. The dataset was obtained from the National Tibetan Plateau Data Center (https://data.tpdc.ac.cn/home; accessed on 15 December 2025). To ensure consistency with other indicators, the nighttime light data were spatially aligned with the study grid, and annual nighttime light intensity values within the 2 km canal buffer were extracted for integrated analysis.

(3) Population density

Population density data were obtained from the GlobPOP global gridded population dataset [34], which was generated using clustering analysis and statistical learning methods. This dataset provides multi-year spatial information on population distribution and was used to characterize baseline population pressure and potential development intensity. The Zenodo version of the dataset was used in this study (https://doi.org/10.5281/zenodo.11179644, accessed on 15 December 2025).

(4) Transportation infrastructure

Transportation data were obtained primarily from the China Surface Transportation GIS Database developed by Davis et al. [35] and accessed through the NBER website (https://www.nber.org/; accessed on 15 December 2025). This database provides annual transportation network data for highways (including expressways), railways (including high-speed rail), and inland waterways for the period 1993–2020, and was used as the main

source for characterizing transport connectivity, infrastructure concentration, and persistent engineering disturbance along the canal corridor. For 2021–2024, transportation infrastructure information was further supplemented using OpenStreetMap (OSM) to extend the annual road network series. To maintain interannual comparability, the OSM-derived road data were processed under the same spatial framework as the original transportation dataset, including alignment to the canal corridor, segment-based aggregation, and the calculation of road-density indicators consistent with those derived from the earlier annual transport data. Based on these combined data, annual road density and transportation network intensity indicators were calculated for the full study period from 1995 to 2024.

Through the above processing, comparable human activity indicators were obtained at a unified spatial scale of 1 km and within a consistent buffer extent, including impervious surface fraction, nighttime light intensity, population density, and transportation network intensity. These variables provided the basis for subsequent principal component analysis (PCA) to construct the Human Activity Intensity Index (HAI) and for coupling analysis with natural risk [19,20].

2.3. Methods

To provide a theoretical basis for the quantitative assessment of natural risk and anthropogenic pressure along the Grand Canal heritage corridor, this study first establishes a conceptual framework of the dual influences of natural and human drivers on the Beijing–Hangzhou Grand Canal (Figure 2). Within this framework, climate change is understood to affect the heritage environment primarily through hazard processes such as extreme heat, intense precipitation, and drought, which influence thermal–moisture balance, hydrological support, and surface stability along the corridor. Human activities, by contrast, alter landscape patterns, development intensity, and ecological buffering conditions through pathways such as urban expansion, population concentration, land-use transformation, and road construction. Together, these two domains influence both the environmental stability of the heritage corridor and its capacity to sustain heritage values. On this basis, the study adopts canal segments as the common assessment units, constructs indicator systems for natural risk and anthropogenic pressure, analyzes their spatiotemporal response characteristics from 1995 to 2024, and further identifies dominant driving types through coupling-based classification, ultimately producing a priority inventory of high-risk canal sections and key heritage sites. The overall technical workflow of the proposed GIS-based spatiotemporal assessment framework is illustrated in Figure 3.

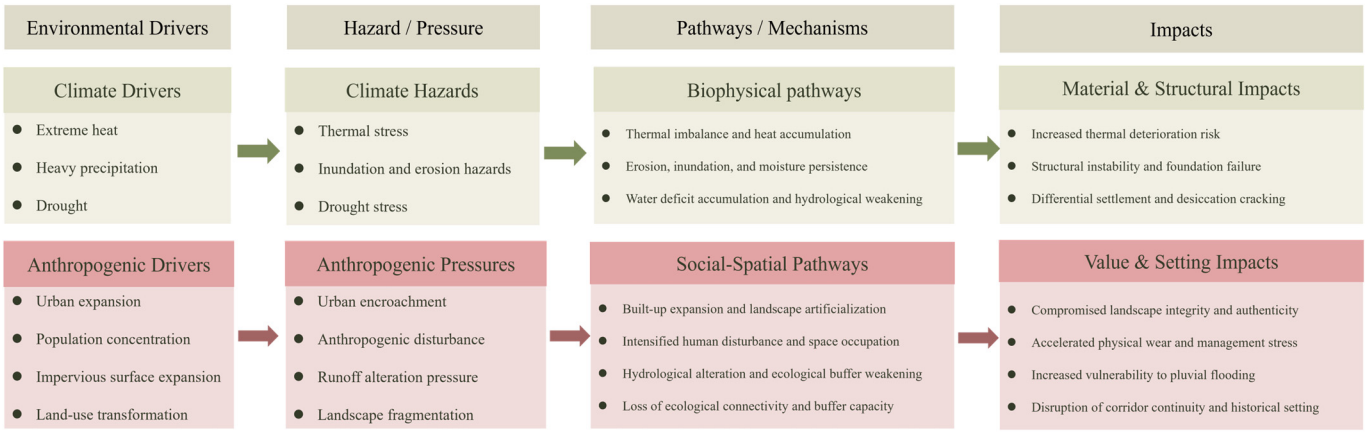


Figure 2. Conceptual framework of climate and anthropogenic drivers, impact pathways, and heritage effects along the Beijing–Hangzhou Grand Canal.

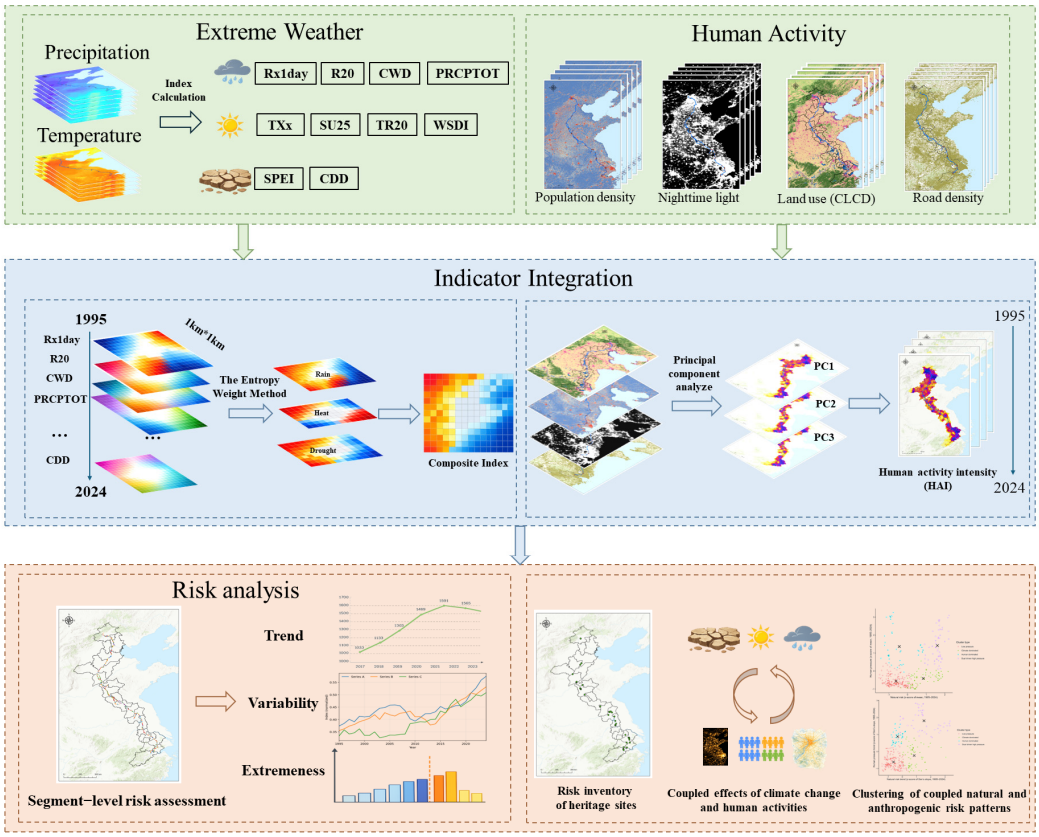


Figure 3. Methodological framework for integrated risk assessment under dual climate and anthropogenic pressures.

2.3.1. Construction of Spatial Units and Data Preprocessing

As a typical linear cultural heritage corridor, the Beijing–Hangzhou Grand Canal is characterized by long-distance cross-regional extension, pronounced environmental variation along its course, and a dispersed distribution of heritage sites that remains closely associated with the canal environment. To balance corridor continuity, full-corridor comparability, and heritage-object identification, this study constructed a multi-scale spatial unit system integrating canal segments, buffer zones, and heritage sites. Specifically, the canal centerline was used as the basis for continuous segmentation at an interval of 10 km to generate segment-level assessment units. A 2 km buffer zone on both sides of the canal was used to represent the near-channel environmental background of the heritage corridor. Heritage sites distributed along the canal were retained as receptor units for the subsequent spatial identification of high-risk canal sections and priority heritage sites. This spatial organization established a unified analytical framework linking corridor-scale environmental risk assessment with the management of specific heritage objects.

To ensure the comparability of multi-source datasets and the reliability of overlay analysis, meteorological, remote sensing, and socioeconomic data were consistently preprocessed by standardizing the coordinate reference system, spatial extent, and study-area mask, and by resampling and aligning raster datasets from different sources. In addition, data with daily, monthly, and annual temporal resolutions were harmonized and aggregated to the annual scale. Meteorological data were used to calculate ETCCDI extreme climate indices and drought indicators, whereas nighttime lights, population density, impervious surface, and road-density data were organized into comparable annual sequences.

Based on the conceptual framework shown in Figure 2, the integrated risk indicator system was constructed from two dimensions: natural hazard processes and anthropogenic pressure. Natural risk was characterized by three groups of climatic processes,

including heat-related processes, heavy precipitation processes, and drought processes. Anthropogenic pressure was characterized by four dimensions, including urban expansion, population concentration, land-use transition, and road-network development. The representative indicators, characterized processes, and potential impacts of these drivers are summarized in Table 1. Together, the standardized spatial units and harmonized datasets provided a consistent data foundation for quantifying natural risk and anthropogenic pressure at the canal-segment scale over the period 1995–2024.

Table 1. Major natural and anthropogenic driver types, representative indicators, and their potential impacts on the Grand Canal heritage corridor.

Driver Type	Representative Indicators	Characterized Process	Potential Impacts on the Grand Canal Heritage Corridor	References
Heat-related process	TXx SU25 TR20 WSDI	Extreme intensity, frequency, and persistence	Thermal aging, material expansion/contraction, moisture imbalance	[3,36,37]
Heavy precipitation process	Rx1day R20 CWD PRCPTOT	Storm intensity, persistence, and wetness	Flooding, scour/erosion, waterlogging, slope instability	[38–40]
Drought process	CDD SPEI-6	Consecutive dry days and water deficit	Soil cracking, hydrological loss, weakened ecological buffering	[41,42]
Urban expansion	NTL	Built-up expansion and socioeconomic intensity	Landscape artificialization, intensified environmental disturbance	[43–45]
Population concentration	POP	Agglomeration and land development demand	Settlement expansion, resource use pressure, activity disturbance	[5,46]
Land-use transition	LULC	Spatial pattern transformation	Landscape fragmentation, weakened integrity and buffer capacity	[8]
Road network	Road density	Infrastructure and accessibility	Engineering disturbance, land fragmentation, environmental discontinuity	[47]

2.3.2. Natural Risk Characterization

Because the natural environmental risk faced by the Grand Canal heritage corridor is not determined by a single climatic factor, but rather by the combined effects of multiple extreme climate processes, this study selected extreme heat, heavy precipitation, and drought as the core dimensions of natural risk characterization. These three processes represent thermal stress, moisture-related disturbance, and water deficit, respectively, and together cover the major climatic pressures affecting heritage environments along the canal. In addition, they provide relatively complete long-term records and good spatial comparability at the full-corridor scale, making them suitable for continuous assessment over 1995–2024. By contrast, factors such as wind, humidity, and freeze–thaw processes were not included because their effects are more region-specific and less comparable across the entire corridor.

Accordingly, extreme heat was represented by TXx, SU25, TR20, and WSDI, heavy precipitation by Rx1day, R20, CWD, and PRCPTOT, and drought by CDD and SPEI-6. These indicators together characterize the major natural hazard processes affecting the Grand Canal heritage corridor in terms of intensity, frequency, and persistence (Table 2).

Table 2. Definitions of the ten candidate extreme climate and drought indices.

Change Type	Index	Definition
Drought	SPEI-6	Standardized Precipitation Evapotranspiration Index at the 6-month timescale (annual minimum), representing the intensity of medium-term moisture deficit
	CDD	Consecutive Dry Days: the maximum number of consecutive days in a year with daily precipitation < 1 mm
Precipitation	CWD	Consecutive Wet Days: the maximum number of consecutive days in a year with daily precipitation ≥ 1 mm
	PRCPTOT	Annual total wet-day precipitation (calculated only for wet days with daily precipitation ≥ 1 mm)
	R20	Number of heavy precipitation days: the annual count of days with daily precipitation ≥ 20 mm
	Rx1day	Annual maximum 1-day precipitation
Temperature	SU25	Number of summer days: the annual count of days with daily maximum temperature > 25 °C
	TR20	Number of tropical nights: the annual count of days with daily minimum temperature > 20 °C
	TXx	Annual maximum of daily maximum temperature
	WSDI	Warm Spell Duration Index: the annual count of days belonging to periods of at least 6 consecutive days when daily maximum temperature exceeds the 90th percentile

To reduce information redundancy and double counting in the integrated natural risk index, the candidate indicators were first tested for inter-indicator correlation and multicollinearity. Pearson's correlation coefficient was used to examine pairwise relationships [48,49], and indicators with $|r| > 0.7$ were considered strongly correlated and were further screened according to their physical meaning and representativeness. Multicollinearity was then evaluated using the Variance Inflation Factor (VIF) [48–50]:

$$VIF_j = \frac{1}{1 - R_j^2} \quad (1)$$

where R_j^2 is the coefficient of determination obtained by regressing indicator j against the remaining indicators. A threshold of VIF > 5 was used to identify severe multicollinearity, and indicators were iteratively removed or replaced until all retained variables satisfied this criterion.

After indicator screening, the entropy weight method was applied to calculate indicator weights and construct the integrated natural risk index [51–53]. After direction adjustment, all indicators were normalized using min–max scaling based on the full spatiotemporal range of the study period (1995–2024) to ensure interannual comparability. The standardized indicators were then combined as follows:

$$R_i = \sum_{j=1}^{n} w_j z_{ij} \quad (2)$$

where R_i is the integrated natural risk value, w_j is the weight of indicator j, and z_{ij} is the standardized value of indicator j for sample i. To ensure interannual comparability, a single set of entropy-based weights was applied to all yearly calculations from 1995 to 2024. Furthermore, to facilitate comparison of the contribution of each sub-indicator to the integrated index, the total contribution weight of each sub-indicator was calculated as $w_j^{total} = W_k \cdot w_{j|k}$. This step allows for a more granular identification of the primary drivers within the natural risk dimension.

It should be noted that entropy-derived weights were interpreted as statistical weights reflecting the discriminatory ability of each indicator within the spatiotemporal dataset, rather than as direct measures of the absolute physical destructiveness of each climatic process to heritage materials. A higher entropy weight indicates that an indicator contributes more strongly to distinguishing spatial and temporal differences in the integrated natural-risk index. Therefore, the entropy-weighted index was used as a data-driven representation of spatiotemporal risk differentiation, while the physical implications of individual indicators were interpreted together with their specific hazard mechanisms.

To examine whether the integrated natural-risk pattern was sensitive to the entropy-derived weights, especially the relatively high weight assigned to persistence-related indicators, two alternative weighting schemes were further used for robustness checking: an equal-weighting scheme and a module-equal-weighting scheme. The resulting natural-risk indices were compared with the entropy-weighted index using Spearman's rank correlation coefficient and the overlap ratio of the top 10% high-risk canal sections.

2.3.3. Anthropogenic Pressure Characterization

To characterize anthropogenic disturbance along the Grand Canal heritage corridor, this study selected four representative dimensions: urban expansion, population concentration, land-use transition, and road network development, represented by nighttime lights (NTL), population density (POP), land use/land cover (LULC), and road density, respectively. Together, these indicators reflect built-environment expansion, the concentration of socioeconomic activities, changes in spatial land use, and increasing infrastructure accessibility.

Because these indicators differ in units, distributions, and interrelationships, principal component analysis (PCA) was used to integrate them into a composite Human Activity Intensity Index (HAI) [50,54,55]. To ensure interannual comparability for 1995–2024, PCA was fitted using the standardized full-period sample rather than being performed separately for each year. The k-th principal component is expressed as

$$PC_k = \sum_{j=1}^{p} a_{kj} z_j \tag{3}$$

where p is the number of indicators, a_{kj} is the loading of indicator j on principal component k, and z_j is the standardized value of indicator j. Principal components with eigenvalues greater than 1 and a cumulative contribution rate of at least 80% were retained to construct the HAI framework.

2.3.4. Spatiotemporal Response Analysis

After obtaining annual natural risk and anthropogenic pressure indices for 1995–2024, their spatiotemporal characteristics were analyzed from three aspects: long-term pattern, interannual variability, and temporal trend. Specifically, long-term patterns refer to the multi-year average state, providing a spatial baseline of risk intensity; temporal trends represent the directional rate of change over time (e.g., Sen's slope); and interannual variability captures the year-to-year fluctuations and stability around the mean. Distinguishing these

dimensions allows for a more nuanced identification of whether a heritage section is facing persistent high pressure or rapidly emerging new threats.

First, the multi-year mean was used to represent the long-term spatial pattern of natural risk and anthropogenic pressure, thereby identifying sections under persistent high-pressure conditions. To further capture temporal instability, the standard deviation (SD) and coefficient of variation (CV) were calculated, allowing for the identification of both high-risk areas and highly variable areas.

Second, because environmental and socioeconomic time series may exhibit non-normal distributions and outliers, the Mann–Kendall (MK) test and Sen's slope estimator were used to assess trend direction, magnitude, and significance [56]. Sen's slope is defined as

$$Q_{ij} = \frac{Y_j - Y_i}{j - i} \tag{4}$$

$$\beta_{Sen} = median(Q_{ij}), 1 \le i < j \le n \tag{5}$$

where β_{Sen} is expressed in units of index per year. Positive values indicate increasing risk, whereas negative values indicate decreasing risk. Trends were classified as significant or non-significant at $\alpha = 0.05$.

Based on these analyses, the spatiotemporal response of the Grand Canal heritage corridor was characterized from the two dimensions of state and change, providing a consistent basis for the subsequent coupling analysis of natural risk and anthropogenic pressure.

2.3.5. Identification of Dominant Driving Types and Priority Inventory Generation

Based on the spatiotemporal response analysis of natural risk and anthropogenic pressure, a coupling feature space was further constructed, and K-means clustering was applied to identify dominant driving types among canal sections [51,53]. The input variables included the multi-year mean natural risk, multi-year mean anthropogenic pressure, natural risk trend, and anthropogenic pressure trend. All input variables were standardized before constructing the segment-level coupling matrix.

The K-means objective function is

$$J = \sum_{k=1}^{K} \sum_{x_i \in C_k} |x_i - \mu_k|^2 \tag{6}$$

where K is the number of clusters, C_k is the k-th cluster, x_i is the sample, and μ_k is the cluster centroid. By minimizing within-cluster variance, canal sections can be objectively grouped without relying on subjective thresholds.

Based on the clustering results and the relative levels of natural risk and anthropogenic pressure, the canal sections were further classified into four dominant driving types: low-pressure stable, natural-dominated, human-dominated, and dual high-pressure. On this basis, high-risk canal sections were identified by combining integrated risk level, trend characteristics, and coupling type. Through spatial overlay analysis between heritage sites and high-risk canal sections, key heritage sites located within or adjacent to these sections were extracted, and a priority inventory of high-risk canal sections and key heritage sites was established to support inspection, conservation prioritization, and spatially differentiated management.

By combining long-term mean conditions and trend information in a standardized feature space, the coupling matrix captures both baseline spatial differentiation and ongoing temporal intensification among canal segments, thereby supporting comparable corridor-scale classification.

3. Results

3.1. Indicator Correlation Screening and VIF Testing

Because strong correlations may exist among different extreme climate indices and drought indicators, multicollinearity can introduce information redundancy and thereby weaken the interpretability of the integrated climate hazard index and subsequent analyses. To reduce this effect, the candidate indicators were first screened through correlation analysis by identifying and ranking indicator pairs with correlation coefficients greater than 0.7 or less than −0.7 [18]. Among strongly correlated indicators, those showing the highest overall correlation with other variables and the greatest overlap in physical meaning were preferentially removed, so as to retain a set of indicators that could represent different types of extreme processes (Figure 4). The correlation analysis showed that the precipitation-related indicators PRCPTOT and R20 were strongly correlated ($|r| > 0.7$). To avoid redundancy between total amount and event frequency information, R20, which directly represents the frequency of heavy precipitation events, was retained in the precipitation subsystem, whereas PRCPTOT was excluded.

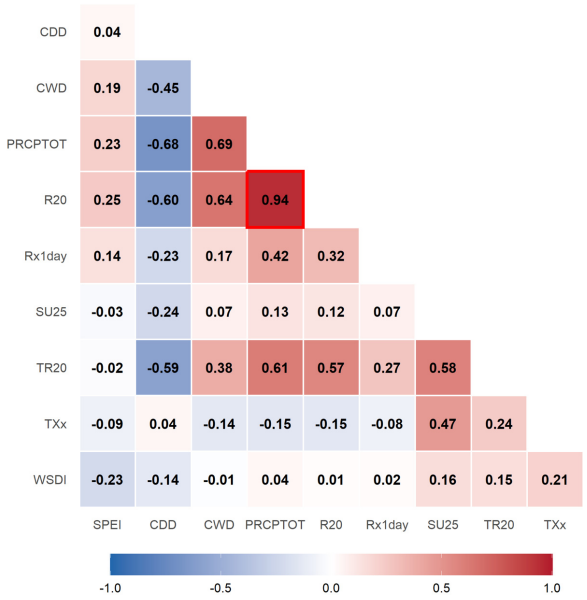


Figure 4. Correlation coefficient matrix of climate indices.

On this basis, the screened indicator set was further tested for multicollinearity using the Variance Inflation Factor (VIF). The VIF results were as follows: TR20 (2.88), R20 (2.85), CDD (1.94), SU25 (1.94), CWD (1.76), TXx (1.45), SPEI6_min (1.22), Rx1day (1.16), and WSDI (1.12). All VIF values were well below the commonly used threshold (VIF < 5), indicating that no significant multicollinearity was present among the selected indicators. These variables were therefore considered suitable for constructing the integrated climate hazard indicator system for the Beijing–Hangzhou Grand Canal and for subsequent risk assessment analyses.

3.2. Indicator Integration

3.2.1. Climate Risk

A two-level entropy weighting method was applied to objectively assign weights to the natural risk indicators (Table 3). First, entropy weights were calculated for the sub-indicators within each module to generate module-level indices (first-level weighting). Second, entropy weights were recalculated among the three module indices—temperature, precipitation, and drought—to obtain module weights (second-level weighting), which

were then used to construct the integrated natural risk index [51,53]. The second-level weighting results show clear differences in the contribution of the three modules to overall risk: the temperature-extreme module received the highest weight ($W_{Temp} = 0.594$), followed by the precipitation-extreme module ($W_{Precip} = 0.242$) and the drought module ($W_{Drought} = 0.164$). This indicates that, at the full-period (1995–2024) and full-corridor scale, temperature-related extremes have greater explanatory power for the spatial pattern of integrated natural risk, suggesting that heat-related processes are the dominant climatic background factor underlying risk differentiation in the study area.

Table 3. Summary of hierarchical weights derived from the two-level entropy weighting method (1995–2024).

Module	Sub-Indicator	First-Level Entropy Weight	Second-Level Entropy Weight	Total Weight
Temperature	WSDI	0.710	0.594	0.422
	TR20	0.109		0.065
	TXx	0.103		0.061
	SU25	0.078		0.046
Precipitation	CWD	0.426	0.242	0.103
	Rx1day	0.298		0.072
	R20	0.276		0.067
Drought	CDD	0.674	0.164	0.110
	SPEI6	0.326		0.054

The first-level entropy weighting results within the temperature module show that WSDI received a substantially higher weight than the other temperature sub-indicators ($w_{WSDI|Temp} = 0.71$), whereas TR20, TXx, and SU25 were assigned relatively lower weights (0.109, 0.103, and 0.078, respectively). The results show that the total contribution weight of WSDI reached 0.422, which was substantially higher than those of the other temperature indicators within the same module. This result indicates that WSDI provided stronger discriminatory information for distinguishing long-term heat-risk differences among canal sections in the present spatiotemporal dataset. However, this statistical contribution should not be interpreted as evidence that sustained warm periods are necessarily more destructive to heritage materials than single-day extreme temperature peaks. TXx was retained in the indicator system because short-term extreme temperature peaks may cause thermal shock, rapid thermal expansion–contraction, and abrupt material stress in heritage structures, whereas WSDI reflects persistent heat exposure and long-term thermal-background pressure. These two indicators therefore characterize different heat-related risk mechanisms.

The precipitation module received a moderate overall weight ($W_{Precip} = 0.242$). Within this module, CWD (consecutive wet days) had the highest internal weight ($w_{CWD|Precip} = 0.426$), followed by Rx1day (0.298) and R20 (0.276). Their corresponding total contribution weights were 0.103, 0.072, and 0.067, respectively. These results suggest that precipitation-related risk differences in the study area are associated not only with the intensity of extreme rainfall, but more prominently with the persistence of wet conditions.

The drought module received a relatively low overall weight ($W_{Drought} = 0.164$), but its internal weighting pattern was clearly concentrated. CDD (consecutive dry days) received a higher weight than SPEI-6 ($w_{CDD|Drought} = 0.674$), with corresponding total contribution weights of 0.110 and 0.054, respectively. This indicates that, compared with

the integrated moisture-balance representation provided by SPEI, drought-related risk differences in the study area are more strongly reflected in the persistence of dry conditions.

A comparison of the total contribution weights across all sub-indicators shows that persistence-related indicators, such as WSDI, CWD, and CDD, contributed more strongly to the statistical differentiation of the integrated natural-risk index. This pattern suggests that persistent background stress was important for explaining the long-term spatial differentiation of natural risk along the Grand Canal. Nevertheless, single-event intensity indicators, such as TXx and Rx1day, remain physically meaningful because short-duration extreme events may produce abrupt thermal or hydrological impacts on heritage materials and their surrounding environments. Therefore, the entropy-weighted index was interpreted as a composite measure of spatiotemporal risk differentiation, rather than as a direct ranking of the physical destructiveness of different hazard processes.

To further examine whether the integrated natural-risk pattern was overly dependent on the relatively high entropy-derived weight of WSDI, two alternative weighting schemes were used for robustness checking: an equal-weighting scheme and a module-equal-weighting scheme. At the multi-year mean segment scale, the Spearman correlation coefficients between the entropy-weighted index and the equal-weighted and module-equal-weighted indices were 0.960 and 0.937, respectively, with both correlations significant at $p < 0.001$. The corresponding overlap ratios of the top 10% high-risk canal sections were 74.29% and 82.86%. These results indicate that the main spatial conclusions, including the north–south risk gradient and the identification of high-risk canal sections, were robust to alternative weighting schemes and were not solely determined by the high entropy-derived weight of WSDI. The detailed robustness results are provided in Table S1.

3.2.2. Anthropogenic Pressure Integration

Based on four indicators—impervious surface fraction, road density, population density, and nighttime lights—this study constructed a composite Human Activity Intensity Index using principal component analysis. To ensure interannual comparability, PCA was not fitted separately for each year. Instead, samples from all years between 1995 and 2024 were pooled and fitted once to obtain a fixed loading matrix and centering parameters. These parameters were then used to project each annual dataset and generate yearly PC score rasters, ensuring that PC scores from different years were located within the same statistical space and were therefore comparable for interannual analysis and trend detection.

The PCA results across the full study period reveal a clear hierarchy in component explanatory power (Table 4). Notably, the first two components (PC1 and PC2) account for 80.8% of the total variance ($\lambda_1 = 0.605$; $\lambda_2 = 0.203$), effectively condensing the primary structural variations of anthropogenic activity into a manageable dimensionality. Consequently, these two were selected as the foundation for the composite index. The loading profiles further distinguish the functional roles of each component. PC1 functions as a broad proxy for urbanization and built-environment expansion, characterized by high loadings for nighttime lights (0.567) and impervious surfaces (0.541). This alignment suggests that surface sealing and artificial illumination expand in tandem with population and road growth. In contrast, PC2 captures a more differentiated spatial pattern, characterized by a strong negative loading on road density (−0.837) and a positive loading on population density (0.525). This suggests that PC2 identifies a functional divergence between transport infrastructure and residential concentration, which complements the broader urbanization signal of PC1. Specifically, a high PC2 score points to densely populated urban cores where human activity is the primary pressure, while a low PC2 score highlights infrastructure-dominated corridors (e.g., industrial zones or transport hubs) where land fragmentation and physical encroachment by road networks pose the dominant threat to the canal's heritage setting.

This distinction allows for a more nuanced assessment of anthropogenic risks beyond simple urban expansion. PC3 exhibited an opposing loading structure between population density (−0.678) and impervious surface (0.646), accompanied by road density (−0.308), reflecting a secondary contrast between population concentration and built-up or impervious development. However, because its explained variance was relatively low (11.2%), PC3 was not retained as a dominant component in the construction of the integrated index.

Table 4. Principal component loadings and explained variance ratios.

Indicator	PC1	PC2	PC3	PC4
Impervious surface	0.541	0.155	0.646	−0.516
Road density	0.393	−0.837	−0.308	−0.23
Population density	0.481	0.525	−0.678	−0.186
Nighttime lights	0.567	−0.014	0.171	0.806
Explained variance ratio (λ)	0.605	0.203	0.112	0.080

The final HAI was constructed by combining PC1 and PC2, weighted by their explained variance contributions:

$$HAI = \frac{\lambda_1 \cdot PC1 + \lambda_2 \cdot PC2}{\lambda_1 + \lambda_2} \quad (7)$$

where λ_1 = 0.605 and λ_2 = 0.203, corresponding to normalized weights of approximately 0.749 for PC1 and 0.251 for PC2 within the composite framework. In this study, higher HAI values indicate stronger anthropogenic intensity. This procedure produced a temporally comparable annual raster series of HAI for 1995–2024, providing a quantitative basis for subsequent coupling analysis with climate-related risk and for identifying differences among canal sections.

It should be noted that PC2 should not be interpreted independently as a unidirectional human-activity intensity component. Instead, PC2 represents a secondary structural contrast between transportation infrastructure intensity and population concentration. Therefore, the contribution of each original indicator to the final HAI should be interpreted based on the variance-weighted composite expression rather than on the loading of a single principal component. After substituting the PCA loadings into the composite formula, the HAI can be approximately expressed as

$$HAI = 0.444Z_{IMP} + 0.084Z_{RD} + 0.492Z_{POP} + 0.421Z_{NTL} \quad (8)$$

where z represents the standardized value of each indicator. The equivalent coefficients of impervious surface, road density, population density, and nighttime lights are all positive, indicating that all four indicators contribute positively to the final HAI. In particular, the negative loading of road density on PC2 reduces its net coefficient but does not reverse its contribution direction. Therefore, higher road density still corresponds to stronger anthropogenic pressure in the final composite index.

3.3. Spatial Patterns and Temporal Changes in Climate Risk

From 1995 to 2024, the three climate risk types along the Beijing–Hangzhou Grand Canal all exhibited pronounced spatial heterogeneity, but with clearly different dominant patterns (Figure 5). Temperature risk generally increased from north to south, with low values in the northern section, a transition zone in the middle section, and a continuous high-value cluster in the southern section. Precipitation risk showed a similar pattern,

also characterized by higher values in the south and lower values in the north, with major high-risk areas concentrated in the middle-lower reaches and southern section. By contrast, drought risk displayed the opposite pattern, with generally higher values in the north and lower values in the south. The northern section and parts of the upper-middle reaches formed the main high-risk areas, whereas the middle-lower reaches and southern section were dominated by lower values. These results indicate a clear spatial division in the effects of different climatic hazard processes along the Grand Canal heritage corridor: temperature and precipitation risks are concentrated mainly in the south, whereas drought risk is more pronounced in the north.

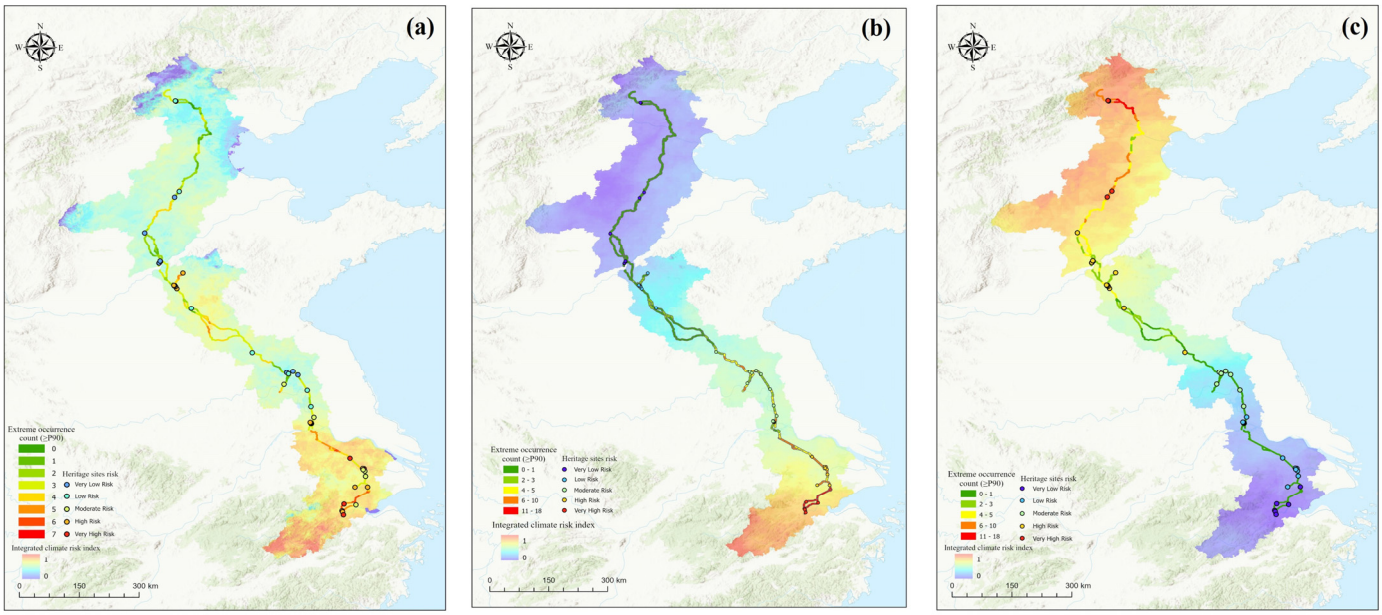


Figure 5. Mean patterns and frequency of extreme high-risk occurrence for temperature, precipitation, and drought risk along the Beijing–Hangzhou Grand Canal, 1995–2024: (**a**) temperature risk; (**b**) precipitation risk; and (**c**) drought risk.

The frequency of extreme high-risk occurrence (≥P90) further reinforces these patterns (Figure 5). High-frequency areas of temperature and precipitation risk largely coincide with their high-mean areas and are mainly distributed in the southern section and parts of the middle-lower reaches (Figure 5a,b), indicating repeated exposure to extreme conditions in these areas. By contrast, high-frequency drought-risk areas are concentrated mainly in the northern section and parts of the middle section (Figure 5c), consistent with the north–high, south–low mean pattern.

Overlay analysis further shows that heritage sites located near sections characterized by both high mean risk and high-frequency occurrence of temperature and precipitation risk tend to face relatively high overall risk levels, particularly in the southern section, where some sites are persistently exposed to combined thermal and moisture-related stresses. In contrast, heritage sites within the northern high-drought-risk zone are more vulnerable to persistent moisture deficit and the repeated occurrence of extreme drought years. Overall, relying only on multi-year mean risk is insufficient for assessing heritage environmental pressure. Incorporating the frequency of extreme high-risk occurrence helps identify key sections that may not have the highest mean risk but are repeatedly exposed to extreme years, thereby providing a more targeted basis for priority section identification and heritage-site conservation.

Considering that different climate risk processes exhibit distinct forms of temporal change, this study focused on the long-term trend of temperature risk, while emphasizing

the interannual variability of precipitation and drought risk (Figure 6). The results show that, from 1995 to 2024, temperature risk along the Grand Canal generally followed an increasing trend, although both the rate and significance of change varied markedly among canal sections. The Sen's slope results indicate that the middle-lower reaches and southern section were generally characterized by relatively strong positive trends, with some stretches forming continuous zones of risk intensification. By contrast, the northern section was dominated by weak increases or non-significant changes, and in some local areas even showed slight declines or near-stable conditions. The significance test further shows that statistically significant increases were concentrated mainly in the middle-lower reaches and southern section, suggesting that the intensification of heat risk was not spatially uniform, but instead mainly superimposed on areas that already had relatively high background risk.

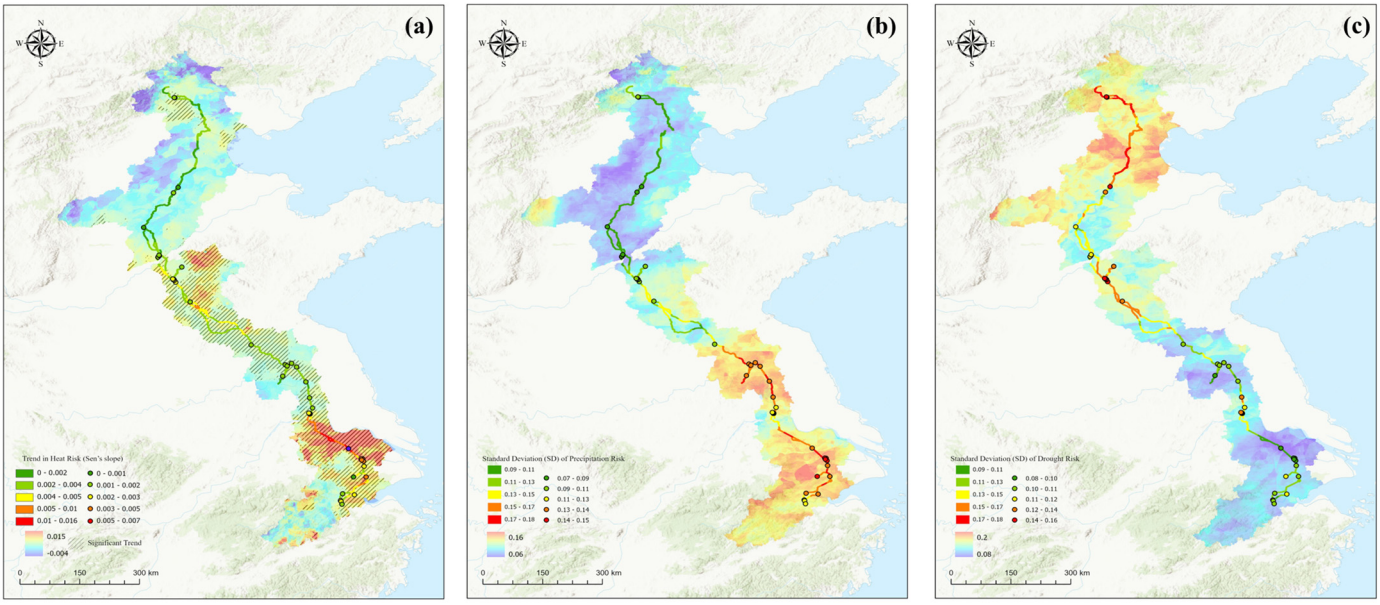


Figure 6. Temporal change characteristics of temperature, precipitation, and drought risk along the Beijing–Hangzhou Grand Canal, 1995–2024: (**a**) trend of temperature risk (Sen's slope); (**b**) interannual variability of precipitation risk (SD); and (**c**) interannual variability of drought risk (SD).

In contrast, the dynamic characteristics of precipitation and drought risk were more prominently reflected in differences in interannual variability. The standard deviation (SD) of precipitation risk showed pronounced spatial heterogeneity along the canal, with relatively high values in the southern section and parts of the middle section. This indicates that these areas experienced greater fluctuations over the multi-year period, with stronger interannual instability and a higher likelihood of unusually severe precipitation impacts in specific years. By comparison, SD values were generally lower in the northern section, suggesting that precipitation risk changed more steadily over time. The SD pattern of drought risk did not fully correspond to its mean distribution. Higher variability occurred in the northern section and parts of the middle section, indicating that these areas not only had relatively high long-term drought risk, but were also more likely to experience rapid increases in drought risk in certain years. In contrast, the southern section showed generally low SD values, suggesting relatively stable drought risk over time.

Overall, the main dynamic characteristic of temperature risk is its continued intensification in the middle-lower reaches and southern section, whereas precipitation and drought risk are better characterized by regional differences in interannual variability. The former reflects the cumulative strengthening of heat risk under a long-term warming background, while the latter reveals the instability and uncertainty of extreme wetness and

moisture-deficit processes across different canal sections. These results suggest that risk identification along the Grand Canal heritage corridor should not rely solely on multi-year mean risk levels, but should also incorporate both trend and variability characteristics in order to distinguish long-term high-pressure areas, persistently intensifying areas, and highly unstable areas.

From 1995 to 2024, integrated natural risk along the Beijing–Hangzhou Grand Canal showed pronounced spatial differentiation, with a clear increase from north to south (Figure 7a). The northern section was generally characterized by a low-risk background, relatively stable conditions, and strong spatial continuity. The middle section mainly represents a transition from low to moderate risk, although some stretches already show localized medium-to-high risk clusters. In the southern section, risk becomes more concentrated and forms a relatively continuous high-risk belt, suggesting long-term exposure to strong compound natural pressures. The distribution of extreme high-risk occurrence broadly matches this pattern. High-risk sections in the south also experienced extreme years more frequently, showing a combined feature of high mean values and high recurrence. In the middle section, some segments were exposed to extreme conditions relatively often even though their mean risk remained moderate. By contrast, the northern section was characterized by low frequencies of extreme high-risk events, consistent with its overall low-risk background. This indicates that combining mean risk with extreme-risk frequency provides a clearer basis for identifying both persistently stressed sections and sections repeatedly affected by extreme years.

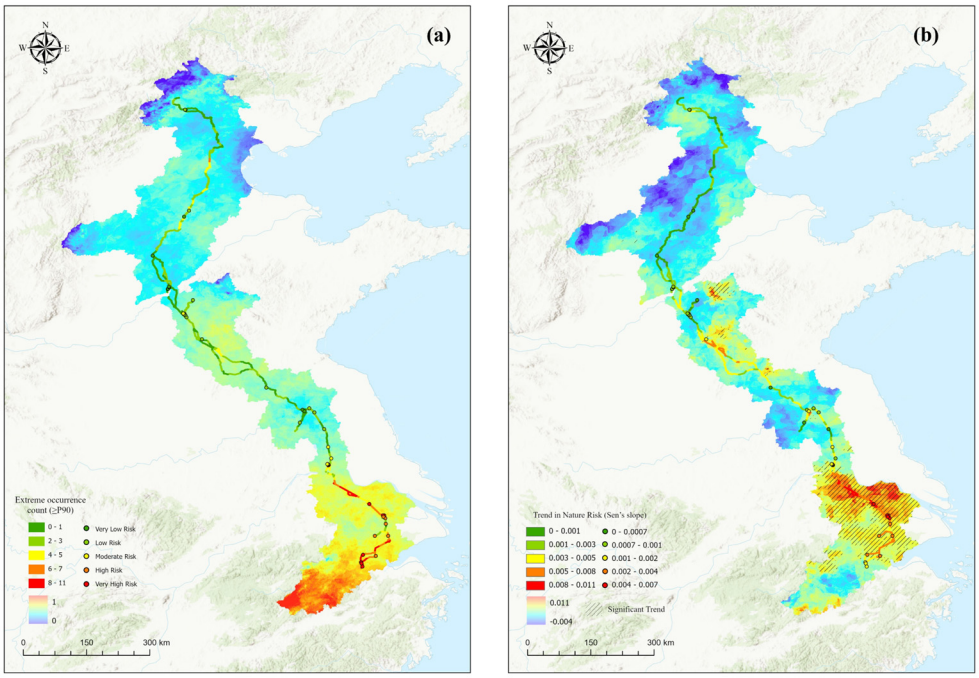


Figure 7. Integrated natural risk, frequency of extreme high-risk occurrence, and trend significance along the Beijing–Hangzhou Grand Canal, 1995–2024: (**a**) integrated natural risk and extreme high-risk frequency; (**b**) integrated natural risk trend (Sen's slope) and significance.

Over the study period, integrated natural risk tended to increase overall, but the rate of change and its statistical significance differed markedly from one canal section to another (Figure 7b). The northern section and parts of the middle section were dominated by weak changes, indicating relatively gradual evolution. Some segments in the middle section showed localized intensification, but the most pronounced increase occurred in the southern section, where trend magnitude, spatial continuity, and statistical significance

were all relatively high. This indicates that the southern section remains under continued intensification on top of an already high-risk background. Taken together, the mean pattern, extreme-frequency pattern, and trend characteristics show that integrated natural risk along the Grand Canal is not static, but reflects the combined effects of long-term high pressure, repeated extreme exposure, and continued intensification. The southern section represents the core high-risk zone, the middle section shows both transitional characteristics and localized hotspots, and the northern section remains under a relatively low-pressure background. These results suggest that natural risk management should focus not only on areas that are currently high-risk, but also on sections where risk is continuing to intensify, so as to support spatially differentiated conservation and adaptive governance.

3.4. Spatial Patterns and Changes in Human Activity Intensity

The multi-year mean of the Human Activity Intensity Index (HAI) derived from principal component analysis was used to represent the overall level of anthropogenic intensity along the canal corridor (Figure 8a). The results show pronounced spatial heterogeneity in human activity intensity, with a clear belt-like clustering pattern along the Grand Canal. High HAI values are concentrated mainly in built-up urban areas, densely populated sections, and transport corridors, indicating sustained human disturbance in these parts of the canal corridor. Low values, by contrast, occur mostly in suburban and mountainous areas farther from major urban centers, where human pressure remains relatively limited.

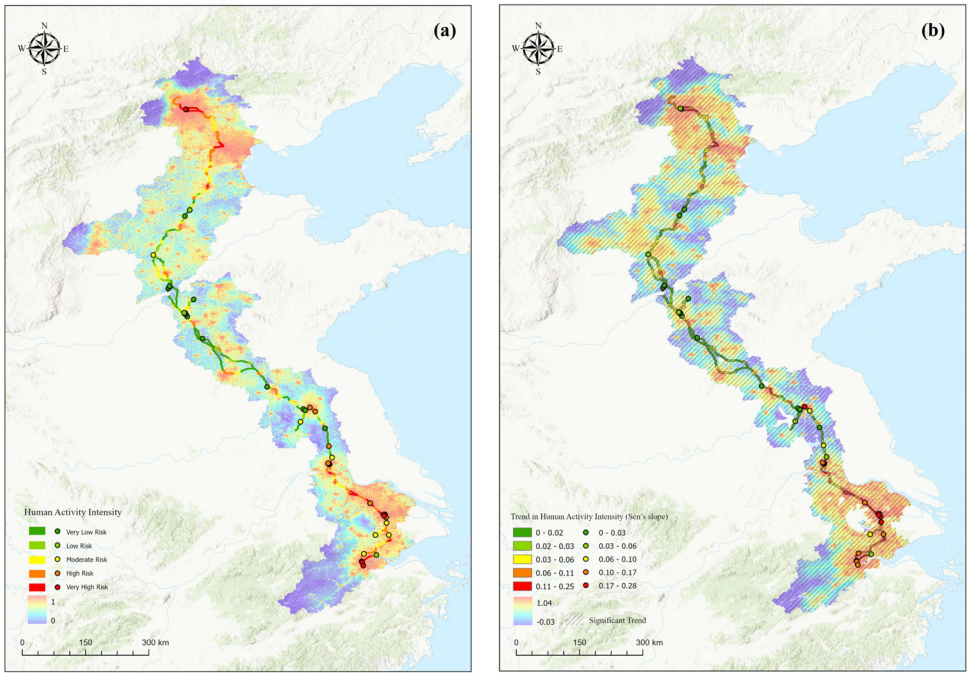


Figure 8. Human activity intensity and its trend significance along the Beijing–Hangzhou Grand Canal, 1995–2024: (**a**) human activity intensity; (**b**) trend of human activity intensity (Sen's slope) and significance.

Further analysis of the HAI series for 1995–2024 using the Mann–Kendall test and Sen's slope estimator shows that human activity intensity generally followed an increasing trend, although the magnitude and significance of growth varied substantially among canal sections (Figure 8b). By combining the multi-year mean intensity with the trend pattern, key sections characterized by both high anthropogenic pressure and continued intensification can be identified, providing a spatial basis for subsequent coupling analysis between natural risk and human activities, as well as for the identification of priority intervention areas.

Figure 9 shows the land-use transitions within the 2 km canal corridor from 1995 to 2024. Overall, the corridor land-use pattern was dominated by persistence, with cropland remaining the principal land-cover type and showing strong long-term stability. At the same time, impervious surfaces increased continuously from 1995 to 2024, with a more pronounced increase in the later period, reflecting the accelerated expansion of built-up areas. Most newly added impervious surfaces were converted from cropland, indicating that urbanization pressure within the corridor has mainly intensified surface sealing through the occupation of agricultural land. This provides direct land-process evidence for the increase in human activity intensity. Water bodies and natural surfaces accounted for relatively small proportions overall, and only limited transitions occurred between these types and cropland or impervious surfaces, suggesting local boundary adjustments rather than large-scale structural reorganization. In general, land-use change within the corridor during 1995–2024 was characterized by the continued dominance of cropland and the sustained expansion of built-up land as the main incremental change, thereby providing an important anthropogenic-process basis for the subsequent identification of dominant driving types between natural risk and human pressure, as well as for the identification of high-risk canal sections.

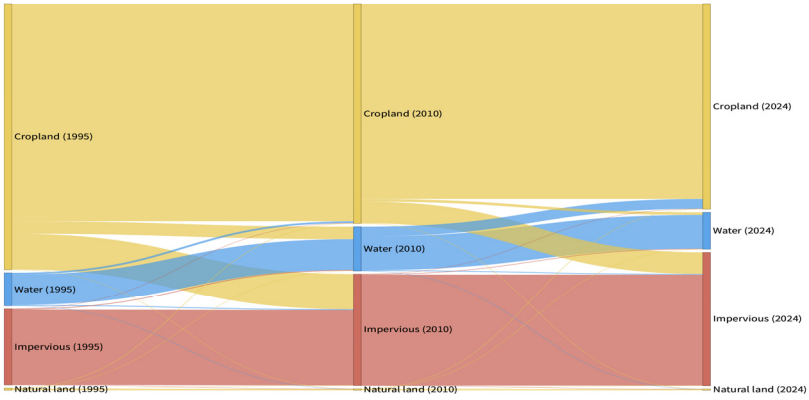


Figure 9. Land-use transition within the 2 km corridor of the Beijing–Hangzhou Grand Canal (1995–2010–2024).

3.5. Coupled Risk Patterns and Dominant Driving Types

Under the combined background of climate change and urbanization, risk along the heritage corridor does not arise from a single pressure source, but is jointly shaped by the coupling of natural risk and anthropogenic pressure. To identify the combined differences among canal sections in terms of long-term risk level and temporal change, and to further locate coupled high-risk hotspots and their dominant driving mechanisms, this study applied K-means clustering to 350 canal sections using four standardized features: the multi-year mean of integrated natural risk and its Sen's slope, and the multi-year mean of anthropogenic pressure and its Sen's slope.

To determine the number of clusters in the K-means analysis, this study jointly applied the elbow method and the mean silhouette coefficient to evaluate clustering performance under different values of K [57]. The elbow method measures clustering compactness using the sum of squared errors (SSE). The results show that SSE decreases rapidly as K increases, but a clear inflection point appears around K = 4 (Figure 10a), indicating that beyond this value, the marginal gain from adding more clusters becomes substantially weaker. The silhouette coefficient was used to assess both within-cluster similarity and between-cluster separability. The results show that the mean silhouette coefficient remains relatively high at K = 4 (Figure 10b), whereas it declines overall when K > 4, suggesting reduced cluster separability. Although smaller values of K may yield slightly higher silhouette

coefficients, such solutions are overly coarse and are insufficient to distinguish the coupled types of natural risk and anthropogenic pressure that are central to this study and their corresponding management implications. Considering both statistical validity and type interpretability, K = 4 was ultimately selected as the optimal number of clusters for the classification of canal-section risk types, and was used for the subsequent identification of dominant driving types and zonal management analysis.

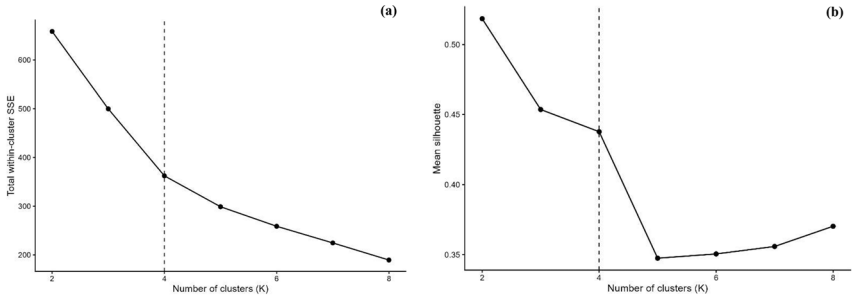


Figure 10. Determination of the optimal number of clusters (K): (**a**) SSE elbow curve; (**b**) average silhouette coefficient.

Figure 11 presents four clustering types of canal sections along the Beijing–Hangzhou Grand Canal under the two-dimensional framework of integrated natural risk and anthropogenic intensity, revealing clear spatial differentiation and segment-based clustering patterns.

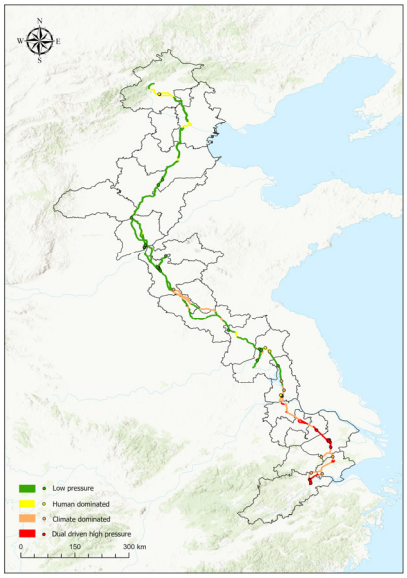


Figure 11. Spatial distribution of dominant driving types for canal sections and heritage sites along the Beijing–Hangzhou Grand Canal.

Overall, the low-pressure type is dominant and is distributed continuously along most of the canal, indicating that both natural risk and anthropogenic pressure remain relatively low or change only gradually in the majority of sections. Against this background, the other three types show localized intensification and patchy clustering broadly consistent with regional development patterns and climatic gradients.

The dual high-pressure type forms relatively continuous hotspot sections mainly in the southern canal, where both natural risk and anthropogenic pressure are high and intensifying. These sections represent the key areas requiring priority intervention and coordinated management. The human-dominated type is mostly distributed in point-like

or short linear clusters, often coinciding with urbanized areas and transport corridors, reflecting the persistent disturbance of urban expansion, land development, and infrastructure concentration. The climate-dominated type occurs in several relatively concentrated sections, indicating that risk in these areas is driven primarily by natural processes such as extreme precipitation, drought, or heat-related change.

Taken together, the figure reveals a corridor pattern characterized by a predominantly low-pressure background, high-pressure concentration in the southern section, elevated anthropogenic intensity around urban nodes, and localized climate-dominated areas. It also provides a spatial basis for differentiated conservation priorities, with the dual high-pressure type representing the main compound-risk hotspot and the other types reflecting secondary spatial risk configurations.

Based on four standardized features—the multi-year mean and Sen's slope of integrated natural risk, and the multi-year mean and Sen's slope of anthropogenic pressure—this study applied K-means clustering (K = 4) to 350 canal sections and visualized the coupling types in a two-dimensional feature space. Figure 12a shows the long-term mean pattern, with standardized integrated natural risk on the *x*-axis and standardized anthropogenic pressure on the *y*-axis. The results identify four coupling types with clear management implications: low-pressure sections in the lower-left quadrant, where both pressures are below average; natural-dominated sections in the lower-right quadrant, where natural risk is high but anthropogenic pressure is relatively weak; human-dominated sections in the upper-left quadrant, where anthropogenic pressure is high but natural risk is relatively low; and dual high-pressure sections in the upper-right quadrant, where both pressures are above average and compound pressure is strongest. Figure 12b further illustrates the long-term rates of change, with the standardized trend of integrated natural risk on the *x*-axis and the standardized trend of anthropogenic pressure on the *y*-axis. The four types remain clearly separated in the trend space. The dual high-pressure type is concentrated in the upper-right area, indicating that both natural risk and anthropogenic pressure are increasing rapidly. Low-pressure sections are located mainly in the lower-left area, showing limited growth in both pressures. Natural-dominated sections show stronger increases in natural risk, whereas human-dominated sections are characterized by faster growth in anthropogenic pressure. Taken together, the two panels identify both long-term high-pressure areas and rapidly intensifying sections, providing a spatial basis for subsequent dominant-driver identification and priority management.

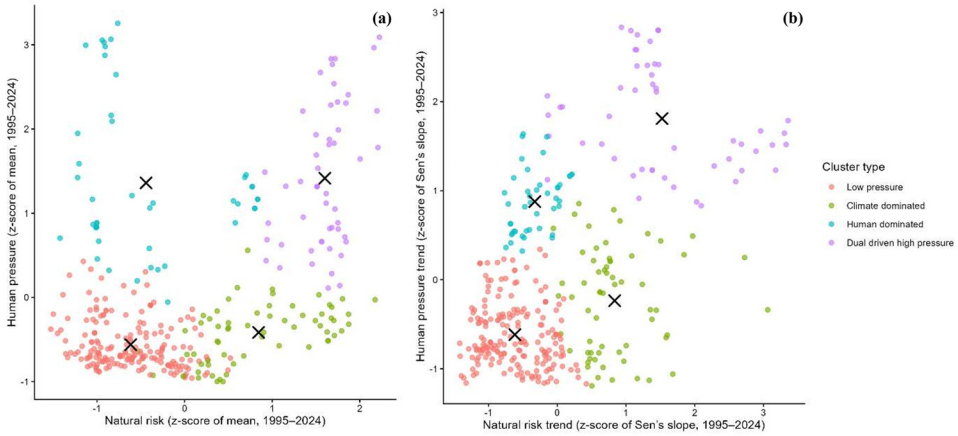


Figure 12. Coupling patterns and clustering results of natural risk and anthropogenic pressure for canal sections along the Beijing–Hangzhou Grand Canal: (**a**) spatial coupling distribution of natural risk and anthropogenic pressure; (**b**) coupling distribution of changes in natural risk and anthropogenic pressure.

3.6. Priority Inventory of Heritage Sites

Through the quantitative assessment of 49 representative heritage sites, the risk pattern along the Beijing–Hangzhou Grand Canal reveals pronounced spatial heterogeneity and asymmetric driving mechanisms (Table 5). At the geographic scale, risk shows a stepwise increase from north to south, reaching its highest level in the Jiangnan Canal section. In the northern canal, particularly in the Cangzhou–Dezhou section and around the Nanwang hub, most heritage elements remain in a relatively stable state characterized by low hazard and low anthropogenic pressure, reflecting comparatively strong environmental resilience and relatively weak urbanization-related disturbance. A clear change begins around the Yangzhou section of the Huaiyang Canal. Here, rising natural risk and increasing anthropogenic pressure occur together, making this area a transition zone of growing risk.

Table 5. Priority inventory of the 49 heritage sites along the Beijing–Hangzhou Grand Canal, with assigned natural-risk and human-activity levels and dominant driving types.

No.	Heritage Element	Natural Risk	Human Activity	Dominant Driving Type
01	Upper Chengqing Lock	Low	Very high	Human-dominated
02	Middle Chengqing Lock	Low	Very high	Human-dominated
03	Shicha Lake	Low	Very high	Human-dominated
04	Xiejia Dam of Lian Town	Low	Low	Low-pressure
05	Rammed Earth Critical Levee at Huajiakou	Very low	Very low	Low-pressure
06	Linqing Customs Post	Very low	Moderate	Low-pressure
07	Lower Echeng Lock	Very low	Very low	Low-pressure
08	Upper Echeng Lock	Very low	Low	Low-pressure
09	Lower Jingmen Lock	Very low	Very low	Low-pressure
10	Upper Jingmen Lock	Very low	Very low	Low-pressure
11	Daicun Dam	Low	Very low	Low-pressure
12	Shili Lock	Low	Low	Low-pressure
13	Doumen Site of Xingtong	Low	Low	Low-pressure
14	Doumen Site of Xujiankou	Moderate	Low	Low-pressure
15	Brick Canal Dike	Low	Low	Low-pressure
16	Liulin Lock	Low	Low	Low-pressure
17	Site of Dragon King's Temple at Water Diversion Point in Nanwang Complex	Low	Very low	Low-pressure
18	Siqianpu Lock	Low	Very low	Low-pressure
19	Lijian Lock	Low	Very low	Climate-dominated
20	Temporary Palace at Dragon King's Temple	Low	Very low	Low-pressure
21	Qingkou Complex	Very low	Very low	Low-pressure
22	Shuangjin Shiplock	Very low	Very low	Low-pressure
23	Qingjiang Shiplock	Low	High	Human-dominated
24	Hongze Lake Levee	Low	Moderate	Low-pressure

Table 5. *Cont.*

No.	Heritage Element	Natural Risk	Human Activity	Dominant Driving Type
25	Site of Caoyun Governor's Mansion	Low	High	Human-dominated
26	Liubao Lock	Low	Very low	Low-pressure
27	Yucheng Post	Moderate	Moderate	Climate-dominated
28	Ancient Shaobo Dyke	Moderate	Moderate	Climate-dominated
29	Shaobo Docks	Moderate	Moderate	Climate-dominated
30	Slender West Lake	Moderate	High	Human-dominated
31	Temporary Palace at Tianning Temple	High	High	Human-dominated
32	Ge Garden	High	High	Human-dominated
33	Wang Lumen's Residence	High	High	Human-dominated
34	Salt Ancestral Temple	High	High	Human-dominated
35	Lu Shaoxu's Residence	High	High	Human-dominated
36	Qingming Bridge Conservation Area	Very high	High	Dual-driven high-pressure
37	Pan Gate	High	Very high	Dual-driven high-pressure
38	Baodai Bridge	High	High	Dual-driven high-pressure
39	Shantang Canal Conservation Area	Very high	Very high	Dual-driven high-pressure
40	Pingjiang Conservation Area	Very high	High	Dual-driven high-pressure
41	Wujiang Ancient Tow Path	High	Moderate	Dual-driven high-pressure
42	Chang'an Lock	High	Low	Climate-dominated
43	Site of Fengshan Water Gate in Hangzhou	Very high	High	Dual-driven high-pressure
44	Hangzhou Fuyi Granary	Very high	High	Dual-driven high-pressure
45	Changhong Bridge	High	Moderate	Climate-dominated
46	Gongchen Bridge	Very high	High	Dual-driven high-pressure
47	Guangji Bridge	Very high	Moderate	Climate dominated
48	Qiaoxi Conservation Area in Hangzhou	Very high	High	Dual-driven high-pressure
49	Nanxun Town Conservation Area	High	Moderate	Climate-dominated

Note: The dominant driving type was assigned according to the K-means clustering results based on four standardized variables (multi-year mean natural risk, natural risk trend, multi-year mean anthropogenic pressure, and anthropogenic pressure trend). The qualitative levels of natural risk and human activity shown in this table are descriptive summaries only and were not used as threshold-based criteria for type assignment.

In terms of dominant drivers, the heritage sites along the canal can be broadly divided into four patterns. The first is a low-pressure pattern, which encompasses the largest share of sites and is distributed mainly across the northern and middle reaches, including the Lubei (Shandong–Hebei) section, the Huitong and Zhonghe canals, and the Nanwang hub area. Representative sites such as the Echeng and Jingmen lock groups, the Linqing Customs Post, and the Nanwang and Qingkou complexes benefit from stable climatic conditions and limited urbanization, thereby retaining strong environmental resilience. The second is a human-dominated pattern, typified by the Beijing section, where risk is primarily driven by urban expansion and the environmental burden of intensive development. The third is a climate-dominated pattern, found in sections between Jiaxing and Hangzhou,

where sites exhibit high sensitivity to extreme precipitation and thermal–moisture fluctuations under the subtropical monsoon climate. The most critical is the dual-pressure coupled pattern, concentrated in the urban cores of Suzhou and Hangzhou. These areas face nonlinear compounding effects from extreme climatic events, high population density, and rapid impervious surface expansion, posing multidimensional challenges to heritage stability.

This four-tier classification provides a scientific basis for the differentiated governance of the Grand Canal as a linear heritage corridor. Rather than a uniform approach, conservation efforts should be progressively scaled: low-pressure sites can be maintained through routine monitoring, while areas dominated by anthropogenic pressure require strict controls over development and construction activities. Most urgently, high-risk sections under compound pressure necessitate the establishment of a preventive conservation system based on dynamic, multi-source monitoring. This management logic directly enhances the resilience and sustainability of the heritage system while optimizing the allocation of limited conservation resources.

4. Discussion

4.1. Main Findings and Geospatial Contributions

This study addresses the Beijing–Hangzhou Grand Canal as a cross-regional, long-distance, and element-rich linear heritage corridor and demonstrates how a GIS-based multi-scale framework can be used to identify coupled climate-related and anthropogenic risks at the corridor scale. Within a unified spatial structure and over the long-term period of 1995–2024, the framework links climate-related hazard, anthropogenic pressure, segment-based classification, and site-level exposure, thereby enabling consistent comparison of both baseline pressure and temporal change along the full canal. The results show that: (1) at the multi-year mean scale, natural risk exhibits pronounced spatial differentiation along the canal, with continuous clusters of high values concentrated in the southern section and parts of the middle section. At the same time, the frequency of extreme high-risk occurrence and interannual variability (SD/CV) do not fully correspond to the mean pattern, indicating that reliance on mean conditions alone may underestimate change-related risk in some canal sections. (2) The two-level entropy weighting results show that the temperature-extreme module makes the largest contribution to integrated natural risk (W_Temp = 0.594), followed by the precipitation and drought modules. The relatively high entropy-derived contribution of persistence-related indicators (WSDI, CWD, and CDD) indicates that these indicators provided strong statistical information for distinguishing spatial risk differentiation. However, this should not be interpreted as a direct ranking of physical destructiveness. Short-duration extreme events, such as TXx and Rx1day, remain important because they may cause abrupt thermal or hydrological stress to heritage materials and their surrounding environments. (3) On the anthropogenic side, a temporally comparable Human Activity Intensity Index (HAI) was constructed using full-period PCA. Its loading structure distinguishes a principal axis of overall urbanization intensity (PC1) from a principal axis of transport infrastructure and road-network intensity (PC2), providing a consistent representation of both the background pattern and long-term growth trend of anthropogenic pressure. (4) Within the coupling feature space of natural risk and anthropogenic pressure, K-means clustering identifies dominant driving types and dual high-pressure hotspots among canal sections without relying on predefined subjective thresholds, thereby improving the spatial interpretation of compound-risk patterns along the corridor.

Compared with previous studies, which have mostly focused on localized heritage sites or individual urban sections, the geospatial contributions of this study are threefold. First, by using canal sections as comparable assessment units, it enables

continuous corridor-scale characterization and further links area-based environmental risk patterns to heritage-site exposure, thereby strengthening the integrated multi-scale representation of site–section–corridor relationships. Second, it incorporates long-term temporal evidence and shows that stable background patterns, extreme-risk frequency, and interannual variability coexist within the same spatial risk structure. Third, it places extreme climate hazard and urbanization-related pressure within a unified quantitative framework and demonstrates how the identification of dominant risk types can support hotspot detection, dominant-driver identification, and spatial decision support in large linear heritage systems.

4.2. Integrating Baseline Spatial Patterns and Temporal Dynamics in Corridor-Scale Risk Assessment

A static view alone is not enough to explain how climate risk and human pressure affect the Grand Canal heritage corridor. For a large linear heritage system such as the Beijing–Hangzhou Grand Canal, risk is shaped not only by long-term spatial differences, but also by the way these pressures change through time. If assessment relies only on conditions in a single year or on multi-year averages, it may identify sections that are already under high pressure, but it can easily miss those where pressure is still rising and future risk is likely to become more severe. For this reason, the present study considers both sides of the problem. One is the relatively stable background pattern, expressed by multi-year levels; the other is temporal change, expressed by long-term trends. Looking at both together makes it easier to understand how risk is formed and why management needs differ from one section to another.

These two aspects do not represent the same thing. Multi-year patterns indicate where heritage sites have long been exposed to persistent climatic stress or continuing human disturbance. Trends, by contrast, show whether those pressures are becoming stronger, weaker, or remaining broadly unchanged. This matters in a linear heritage corridor, because pressure is not confined to existing hotspots. It may accumulate in long-established urban or environmentally sensitive sections, but it may also spread into new areas as climate stress intensifies or development expands along the corridor. If only the spatial pattern is considered, established high-pressure sections are likely to dominate the assessment. If only trends are considered, areas with rapid change but a low baseline may receive too much attention. Combining the two helps separate sections under persistent high pressure from those entering a new phase of risk growth.

This is especially important when natural and anthropogenic pressures are examined together. A classification based only on current intensity can distinguish broad types, but it says little about whether those conditions are stable or still strengthening. Once long-term levels and trends are considered together, it becomes possible to distinguish between sections under long-standing compound pressure and sections where compound risk is building more rapidly. The management implications are different. The former calls for sustained conservation and routine control, whereas the latter requires earlier intervention, closer monitoring, and more forward-looking planning. In this sense, combining static patterns with temporal change does more than improve interpretation. It also makes the resulting priority inventory more useful for differentiated conservation and adaptive governance.

4.3. A Multi-Scale Geospatial Framework of Canal Section–Buffer Zone–Heritage Site

A key methodological contribution of this study is the construction of a multi-scale spatial framework linking canal sections, buffer zones, and heritage sites. This framework bridges area-based environmental assessment and site-based heritage exposure by providing a common spatial support for indicator aggregation, comparison,

and classification along the full corridor. In contrast to point-based or irregular areal representations, segment-based units improve full-corridor comparability and make it possible to trace spatial continuity, local transitions, and corridor-scale clustering within a single analytical structure.

This scale is also closer to actual conservation practice. In practical terms, canal sections can be used as units for inspection, maintenance, and control, while heritage sites remain the focus of exposure assessment and asset protection. Under this framework, the risk inventory does more than show where pressure is high. It also indicates the dominant drivers and whether those pressures are changing, which makes the results more useful for management.

In our view, this is one of the practical strengths of the framework. It creates a clearer basis for setting inspection frequency, prioritizing repair and conservation work, applying differentiated zoning measures, and arranging monitoring sites. In this sense, the assessment is not only descriptive, but also directly useful for moving from risk identification to management action.

4.4. Coupled Spatial Effects of Natural Risk and Anthropogenic Pressure

Figure 13 integrates the segment-based coupling results with evidence from field investigation, providing additional support for the interpretation of compound-risk patterns along the Beijing–Hangzhou Grand Canal. The surveyed sites are distributed across different parts of the canal, and local environmental conditions vary markedly among sections. In some areas, bank hardening, impervious surface expansion, waterfront development, and dense transport infrastructure have already altered shoreline conditions and runoff processes. These changes reduce the buffering capacity of the surrounding environment and increase exposure to heavy rainfall, water-level fluctuations, and related hydro-climatic disturbance. At the same time, persistent wetness, heatwaves, and alternating dry–wet conditions may further intensify material deterioration through repeated saturation, wet–dry cycling, and thermal expansion and contraction.

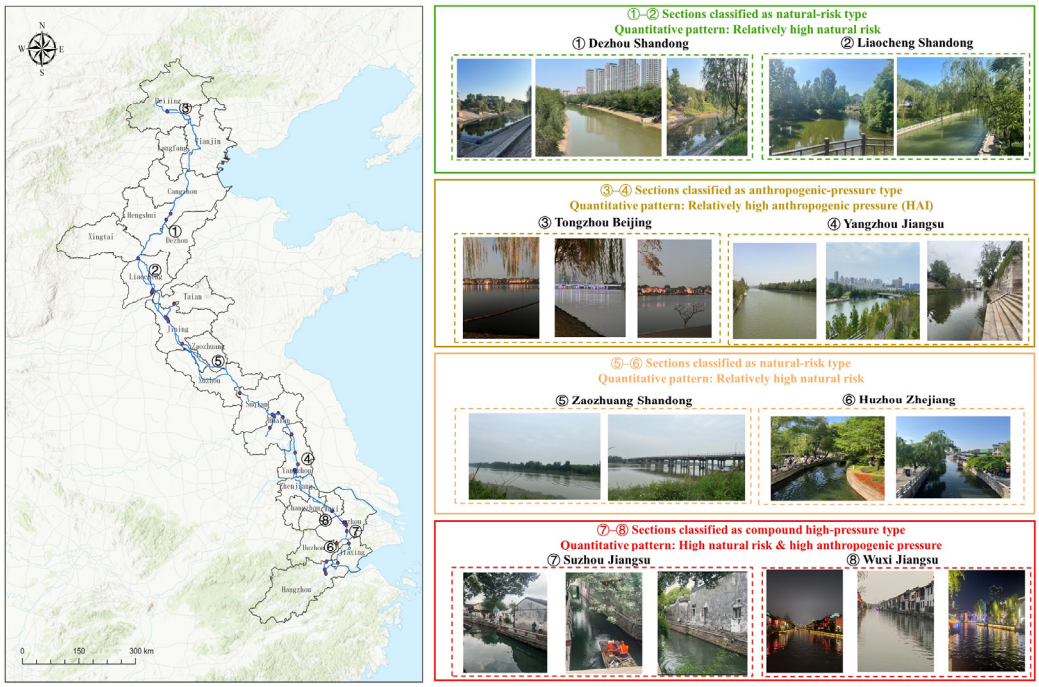


Figure 13. Field photographs supporting the interpretation of dominant driving types along the Beijing–Hangzhou Grand Canal.

The combined evidence indicates that risk along the Grand Canal cannot be adequately explained by either natural risk or anthropogenic pressure alone. Instead, the spatial interaction between the two dimensions produces distinct compound-risk configurations, which differ in both baseline intensity and local expression. Similar natural settings may lead to different levels of vulnerability under different degrees of human disturbance, while sections with comparable development intensity may still diverge in risk because the underlying climatic hazard is not the same. Examining natural risk and anthropogenic pressure together therefore improves the spatial interpretation of why some canal sections emerge as persistent hotspots, while others remain relatively stable or shift toward intensifying compound pressure.

This coupling perspective also helps clarify the spatial logic of differentiated responses. Sections exposed to both high natural risk and strong anthropogenic pressure should be treated as priority areas for intensified monitoring and preventive intervention. In human-dominated sections, the main concern is the continued accumulation of development-related disturbance, whereas climate-dominated sections require greater attention to adaptive measures against hydro-climatic stress. Low-pressure sections can remain under routine monitoring, but still need to be tracked for potential change over time. Taken together, the combination of dominant driving type identification, high-risk section inventories, and field evidence improves the delineation of compound-pressure concentration zones and provides a clearer basis for hotspot detection and spatially differentiated decision support in large linear heritage systems.

4.5. Uncertainty, Scale Effects and Future Extensions

Although the proposed framework provides a consistent basis for corridor-scale risk identification, some uncertainty remains in the integration of multi-source geospatial datasets with different spatial resolutions, temporal coverages, and data-generation mechanisms. In particular, uncertainty may arise during resampling, alignment, and aggregation when heterogeneous climatic, environmental, and socioeconomic indicators are transformed into comparable segment-level variables. In addition, the use of fixed segment-based assessment units improves full-corridor comparability, but may also smooth local heterogeneity in sections where environmental conditions and development intensity change rapidly over short distances. At the current analytical scale, the framework links corridor environments with heritage sites effectively, but does not yet fully distinguish the material-specific responses of different heritage entities under microclimatic stress. Future research could further evaluate the sensitivity of results to spatial unit definition and strengthen the linkage between corridor-scale geospatial assessment and finer-scale evidence on site-specific vulnerability.

5. Conclusions

This study proposes a GIS-based multi-scale spatiotemporal assessment framework for identifying coupled climate-related and anthropogenic risks in a large linear heritage corridor. Using the Beijing–Hangzhou Grand Canal as a case study, the framework integrates canal sections, buffer zones, and heritage sites within a unified spatial structure and enables comparable assessment across approximately 350 canal segments during 1995–2024. The results reveal a stepwise increase in integrated risk from north to south and identify the Jiangnan Canal section as the principal hotspot of compound pressure. By moving beyond single-dimension assessment, the study captures the coupled effects of natural risk and anthropogenic pressure, identifies dominant driving types, and generates a spatially explicit inventory of high-risk canal sections and priority heritage sites. More broadly, the proposed framework shifts the focus of corridor-scale risk assessment from static hazard

overlay to dynamic driver-dominance analysis, and provides a geospatial basis for hotspot detection and spatial decision support in large linear heritage systems under conditions of rapid environmental change.

Supplementary Materials: The following supporting information can be downloaded at https://www.mdpi.com/article/10.3390/ijgi15060230/s1, Table S1: Robustness check of the integrated natural-risk index under alternative weighting schemes.

Author Contributions: Conceptualization, Junyi Shi and Lijun Yu; Methodology, Junyi Shi; Software, Junyi Shi; Validation, Junyi Shi; Formal analysis, Junyi Shi and Lijun Yu; Investigation, Junyi Shi, Lijun Yu, Ze Liu, Hui Wang and Yueping Nie; Data curation, Junyi Shi and Lijun Yu; Writing—original draft, Junyi Shi and Lijun Yu; Writing—review and editing, Junyi Shi, Lijun Yu and Hui Wang; Visualization, Junyi Shi; Supervision, Junyi Shi, Lijun Yu, Ze Liu, Hui Wang and Yueping Nie; Project administration, Lijun Yu and Hui Wang. All authors have read and agreed to the published version of the manuscript.

Funding: This research was funded by the National Key Research and Development Program of China, grant number 2020YFC1521900.

Data Availability Statement: The data presented in this study are available from the corresponding author upon reasonable request. Researchers with relevant academic purposes may contact the corresponding author to obtain the minimal dataset supporting the conclusions of this study. Full public sharing of the complete dataset is limited because this study integrates multiple third-party geospatial, climatic, and human activity datasets, and the long-term multi-source assessment process generated a large volume of raw and intermediate files.

Conflicts of Interest: The authors declare no conflicts of interest.

References

1. Wang, Y. Management of the Grand Canal and It's Bid as a World Cultural Heritage Site. *Front. Archit. Res.* **2012**, *1*, 34–39. [CrossRef]
2. Zhang, S.; Zhang, X.; Liu, J. Spatial Distribution and Pedigree Age of Intangible Cultural Heritage along the Grand Canal of China. *Herit. Sci.* **2024**, *12*, 246. [CrossRef]
3. Chen, Z.; Gao, Q.; Wu, Y.; Li, J.; Li, X.; Li, X.; Wang, Z.; Cui, H. World Cultural Heritage Sites Are under Climate Stress and No Emissions Mitigation Pathways Can Uniformly Protect Them. *Commun. Earth Environ.* **2025**, *6*, 628. [CrossRef]
4. Chen, G.; Fu, B.; Jiang, Y.; Suo, X.; Lai, Y.; Chen, Z.; Li, J.; Li, L.; Lu, M.; Tang, Y.; et al. Natural World Heritage Sites Are at Risk from Climate Change Globally. *Commun. Earth Environ.* **2024**, *5*, 760. [CrossRef]
5. Fu, L.; Zhang, Q.; Tang, Y.; Pan, J.; Li, Q. Assessment of Urbanization Impact on Cultural Heritage Based on a Risk-Based Cumulative Impact Assessment Method. *Herit. Sci.* **2023**, *11*, 177. [CrossRef]
6. Hu, H.; Hewitt, R.J. Understanding Climate Risks to World Cultural Heritage: A Systematic Analysis and Assessment Framework for the Case of Spain. *Herit. Sci.* **2024**, *12*, 194. [CrossRef]
7. Agapiou, A.; Alexakis, D.D.; Lysandrou, V.; Sarris, A.; Cuca, B.; Themistocleous, K.; Hadjimitsis, D.G. Impact of Urban Sprawl to Cultural Heritage Monuments: The Case Study of Paphos Area in Cyprus. *J. Cult. Herit.* **2015**, *16*, 671–680. [CrossRef]
8. Guo, H.; Chen, F.; Tang, Y.; Ding, Y.; Chen, M.; Zhou, W.; Zhu, M.; Gao, S.; Yang, R.; Zheng, W.; et al. Progress toward the Sustainable Development of World Cultural Heritage Sites Facing Land-Cover Changes. *Innovation* **2023**, *4*, 100496. [CrossRef]
9. Crowley, K.; Jackson, R.; O'Connell, S.; Karunarthna, D.; Anantasari, E.; Retnowati, A.; Niemand, D. Cultural Heritage and Risk Assessments: Gaps, Challenges, and Future Research Directions for the Inclusion of Heritage within Climate Change Adaptation and Disaster Management. *Clim. Resil.* **2022**, *1*, e45. [CrossRef]
10. Quesada-Ganuza, L.; Garmendia, L.; Roji, E.; Gandini, A. Do We Know How Urban Heritage Is Being Endangered by Climate Change? A Systematic and Critical Review. *Int. J. Disaster Risk Reduct.* **2021**, *65*, 102551. [CrossRef]
11. Fatorić, S.; Daly, C. Towards a Climate-smart Cultural Heritage Management. *WIREs Clim. Change* **2023**, *14*, e855. [CrossRef]
12. Zhang, Y.; Jing, Z.; Huang, Q.; Wang, X.; Sun, W.; Zhang, C.; Wang, J.; Zhong, Y.; Wang, J.; Tan, L.; et al. On Conservation of World Heritage Beijing-Hangzhou Grand Canal for Enhancing Cultural Ecosystem Services. *Herit. Sci.* **2023**, *11*, 269. [CrossRef]
13. Zhao, M.; Zhou, Y.; Li, X.; Cao, W.; He, C.; Yu, B.; Li, X.; Elvidge, C.D.; Cheng, W.; Zhou, C. Applications of Satellite Remote Sensing of Nighttime Light Observations: Advances, Challenges, and Perspectives. *Remote Sens.* **2019**, *11*, 1971. [CrossRef]

14. Ravan, M.; Revez, M.J.; Pinto, I.V.; Brum, P.; Birkmann, J. A Vulnerability Assessment Framework for Cultural Heritage Sites: The Case of the Roman Ruins of Tróia. *Int. J. Disaster Risk Sci.* **2023**, *14*, 26–40. [CrossRef]
15. Ravankhah, M.; De Wit, R.; Argyriou, A.V.; Chliaoutakis, A.; Revez, M.J.; Birkmann, J.; Žuvela-Aloise, M.; Sarris, A.; Tzigounaki, A.; Giapitsoglou, K. Integrated Assessment of Natural Hazards, Including Climate Change's Influences, for Cultural Heritage Sites: The Case of the Historic Centre of Rethymno in Greece. *Int. J. Disaster Risk Sci.* **2019**, *10*, 343–361. [CrossRef]
16. Cacciotti, R.; Sardella, A.; Drdácký, M.; Bonazza, A. A Methodology for Vulnerability Assessment of Cultural Heritage in Extreme Climate Changes. *Int. J. Disaster Risk Sci.* **2024**, *15*, 404–420. [CrossRef]
17. Sardella, A.; Palazzi, E.; Von Hardenberg, J.; Del Grande, C.; De Nuntiis, P.; Sabbioni, C.; Bonazza, A. Risk Mapping for the Sustainable Protection of Cultural Heritage in Extreme Changing Environments. *Atmosphere* **2020**, *11*, 700. [CrossRef]
18. Kim, J.; Lee, M.-H.; Ahn, J.-H.; Seo, S.B. An Integrated Approach for Characterizing and Selecting Climate Change Scenarios Based on Variability and Extremeness. *Sci. Rep.* **2025**, *15*, 41002. [CrossRef]
19. Yang, J.; You, Y.; Ye, X.; Lin, J. Cultural Heritage Sites Risk Assessment Based on RS and GIS—Takes the Fortified Manors of Yongtai as an Example. *Int. J. Disaster Risk Reduct.* **2023**, *88*, 103593. [CrossRef]
20. Yao, Y.; Wang, X.; Luo, L.; Wan, H.; Ren, H. An Overview of GIS-RS Applications for Archaeological and Cultural Heritage under the DBAR-Heritage Mission. *Remote Sens.* **2023**, *15*, 5766. [CrossRef]
21. Tang, Y.; Shao, Z.; Huang, X.; Cai, B. Mapping Impervious Surface Areas Using Time-Series Nighttime Light and MODIS Imagery. *Remote Sens.* **2021**, *13*, 1900. [CrossRef]
22. Moise, C.; Dana Negula, I.; Mihalache, C.E.; Lazar, A.M.; Dedulescu, A.L.; Rustoiu, G.T.; Inel, I.C.; Badea, A. Remote Sensing for Cultural Heritage Assessment and Monitoring: The Case Study of Alba Iulia. *Sustainability* **2021**, *13*, 1406. [CrossRef]
23. Hu, Q.; Li, S. Spatial Reconstruction and Economic Vitality Assessment of Historical Towns Using SDGSAT-1 Nighttime Light Imagery and Historical GIS: A Case Study of Suburban Shanghai. *Remote Sens.* **2025**, *17*, 2123. [CrossRef]
24. Li, L.; Feng, R.; Xi, J. Ecological Risk Assessment and Protection Zone Identification for Linear Cultural Heritage: A Case Study of the Ming Great Wall. *Int. J. Environ. Res. Public Health* **2021**, *18*, 11605. [CrossRef]
25. Liu, R.; Meng, D.; Wang, M.; Gong, H.; Li, X. Analysis of Spatiotemporal Dynamics and Driving Mechanisms of Cultural Heritage Distribution Along the Jiangnan Canal, China. *Sustainability* **2025**, *17*, 5026. [CrossRef]
26. Cai, J.; Peng, J. Introduction of Beijing-Hangzhou Grand Canal and Analysis of Its Heritage Values. *J. Hydro-Environ. Res.* **2019**, *26*, 2–7. [CrossRef]
27. Ma, X.; Shi, Y.; Zhang, S.; Yang, J.; Guo, L. Analysis of the Impact of Traditional Ethnic Villages in Hani Area on Sustainable Development. *PLoS ONE* **2023**, *18*, e0283142. [CrossRef] [PubMed]
28. Ratnayake, S.S.; Reid, M.; Larder, N.; Hunter, D.; Ranagalage, M.; Kogo, B.; Dharmasena, P.B.; Kariyawasam, C.S. Knowing the Lay of the Land: Changes to Land Use and Cover and Landscape Pattern in Village Tank Cascade Systems of Sri Lanka. *Front. Environ. Sci.* **2024**, *12*, 1353459. [CrossRef]
29. Sun, Y.; Wang, Y.; Liu, L.; Wei, Z.; Li, J.; Cheng, X. Large-Scale Cultural Heritage Conservation and Utilization Based on Cultural Ecology Corridors: A Case Study of the Dongjiang-Hanjiang River Basin in Guangdong, China. *Herit. Sci.* **2024**, *12*, 44. [CrossRef]
30. Hu, Y.; Zhang, L. Added Value of Merging Techniques in Precipitation Estimates Relative to Gauge-Interpolation Algorithms of Varying Complexity. *J. Hydrol.* **2024**, *645*, 132214. [CrossRef]
31. Zhang, L.; Li, X.; Zheng, D.; Zhang, K.; Ma, Q.; Zhao, Y.; Ge, Y. Merging Multiple Satellite-Based Precipitation Products and Gauge Observations Using a Novel Double Machine Learning Approach. *J. Hydrol.* **2021**, *594*, 125969. [CrossRef]
32. Yang, J.; Huang, X. The 30 m Annual Land Cover Dataset and Its Dynamics in China from 1990 to 2019. *Earth Syst. Sci. Data* **2021**, *13*, 3907–3925. [CrossRef]
33. Tian, Y.; Cheng, K.M.; Zhang, Z.; Zhang, T.; Feng, J.; Ren, Z.; Li, S.; Yan, D.; Xu, B. An Extended VIIRS-like Artificial Nighttime Light Data Reconstruction (1986–2024). *Sci. Data* **2026**, *13*, 233. [CrossRef]
34. Liu, L.; Cao, X.; Li, S.; Jie, N. A 31-Year (1990–2020) Global Gridded Population Dataset Generated by Cluster Analysis and Statistical Learning. *Sci. Data* **2024**, *11*, 124. [CrossRef]
35. Davis, S.; Qian, M.; Zeng, W. *A Comprehensive GIS Database for China's Surface Transport Network with Implications for Transport and Socioeconomics Research*; National Bureau of Economic Research: Cambridge, MA, USA, 2025. [CrossRef]
36. Sesana, E.; Gagnon, A.S.; Ciantelli, C.; Cassar, J.; Hughes, J.J. Climate Change Impacts on Cultural Heritage: A Literature Review. *WIREs Clim. Change* **2021**, *12*, e710. [CrossRef]
37. Lobarinhas, R.; Dionísio, A.; Paneiro, G. High Temperature Effects on Global Heritage Stone Resources: A Systematic Review. *Heritage* **2024**, *7*, 6310–6342. [CrossRef]
38. Salazar, L.G.F.; Figueiredo, R.; Romão, X. Flood Vulnerability Assessment of Built Cultural Heritage: Literature Review and Identification of Indicators. *Int. J. Disaster Risk Reduct.* **2024**, *111*, 104666. [CrossRef]
39. Momčilović Petronijević, A.; Petronijević, P. Floods and Their Impact on Cultural Heritage—A Case Study of Southern and Eastern Serbia. *Sustainability* **2022**, *14*, 14680. [CrossRef]

40. Freitas, T.S. The Impact of Floods on Cultural Heritage: Types of Damage, Frequent Treatment Measures, and a New Proposal. *UCL Open Environ.* **2025**, *7*, 1–3. [CrossRef]
41. Yue, J.; Huang, X.; Zhao, L.; Wang, Z. Study on the Factors Affecting Cracking of Earthen Soil under Dry Shrinkage and Freeze–Thaw Conditions. *Sci. Rep.* **2022**, *12*, 1816. [CrossRef]
42. Zhang, Y. Knowledge of Earthen Heritage Deterioration in Dry Areas of China: Salinity Effect on the Formation of Cracked Surface Crust. *Herit. Sci.* **2023**, *11*, 41. [CrossRef]
43. Hu, W.; Zhang, H.; Wu, Y. Urbanization-Driven Risk Assessment of Song-Dynasty Cultural Heritage under Land-Use Transition: A Landscape-Based Spatial Model for Historic Kaifeng, China. *Geomatica* **2025**, *77*, 100086. [CrossRef]
44. Li, Y.; Jia, N.; Yin, C.; Chen, R. Transition of Land Use/Cover in World Heritage Cities under Climate Crisis. *Ecol. Indic.* **2024**, *169*, 112972. [CrossRef]
45. Zou, J.; Deng, Y. Intelligent Assessment System of Material Deterioration in Masonry Tower Based on Improved Image Segmentation Model. *Herit. Sci.* **2024**, *12*, 252. [CrossRef]
46. Méndez, A.; Prieto, B.; i Font, J.M.A.; Sanmartín, P. Better, Not More, Lighting: Policies in Urban Areas towards Environmentally-Sound Illumination of Historical Stone Buildings That Also Halts Biological Colonization. *Sci. Total Environ.* **2024**, *906*, 167560. [CrossRef]
47. Zini, G.; Betti, M.; Bartoli, G. Experimental Analysis of the Traffic-induced-vibration on an Ancient Lodge. *Struct. Control. Health Monit.* **2022**, *29*, e2900. [CrossRef]
48. Arenas-Castro, S.; Regos, A.; Gonçalves, J.F.; Alcaraz-Segura, D.; Honrado, J. Remotely Sensed Variables of Ecosystem Functioning Support Robust Predictions of Abundance Patterns for Rare Species. *Remote Sens.* **2019**, *11*, 2086. [CrossRef]
49. Zhang, Y.; Wei, Y.; Yao, R.; Sun, P.; Zhen, N.; Xia, X. Data Uncertainty of Flood Susceptibility Using Non-Flood Samples. *Remote Sens.* **2025**, *17*, 375. [CrossRef]
50. Romero-Sanchez, M.; Ponce-Hernandez, R. Assessing and Monitoring Forest Degradation in a Deciduous Tropical Forest in Mexico via Remote Sensing Indicators. *Forests* **2017**, *8*, 302. [CrossRef]
51. Xu, H.; Ma, C.; Lian, J.; Xu, K.; Chaima, E. Urban Flooding Risk Assessment Based on an Integrated K-Means Cluster Algorithm and Improved Entropy Weight Method in the Region of Haikou, China. *J. Hydrol.* **2018**, *563*, 975–986. [CrossRef]
52. Li, J.; Chen, Y.; Yao, X.; Chen, A. Risk Management Priority Assessment of Heritage Sites in China Based on Entropy Weight and TOPSIS. *J. Cult. Herit.* **2021**, *49*, 10–18. [CrossRef]
53. Zheng, C.; Yang, W.; Jiang, X.; Lian, J.; Hu, D.; Yan, X.; Yan, L. A Novel Integrated Urban Flood Risk Assessment Approach Coupling GeoDetector-Dematel and Clustering Method. *J. Environ. Manag.* **2024**, *354*, 120308. [CrossRef] [PubMed]
54. Zhang, K.; Feng, R.; Zhang, Z.; Deng, C.; Zhang, H.; Liu, K. Exploring the Driving Factors of Remote Sensing Ecological Index Changes from the Perspective of Geospatial Differentiation: A Case Study of the Weihe River Basin, China. *Int. J. Environ. Res. Public Health* **2022**, *19*, 10930. [CrossRef] [PubMed]
55. Xie, W.; Yao, Y. High-Quality Human Activity Intensity Maps in China From 2000 to 2020. *Glob. Ecol. Biogeogr.* **2025**, *34*, e70130. [CrossRef]
56. Ahmad, I.; Tang, D.; Wang, T.; Wang, M.; Wagan, B. Precipitation Trends over Time Using Mann-Kendall and Spearman's Rho Tests in Swat River Basin, Pakistan. *Adv. Meteorol.* **2015**, *2015*, 431860. [CrossRef]
57. Zhang, S.; Yang, Z.; Wang, C. Environmental Risk Assessment of Earthen Heritage Sites in Arid Regions: A Case Study of the Great Wall in Xinjiang. *npj Herit. Sci.* **2025**, *13*, 200. [CrossRef]

Disclaimer/Publisher's Note: The statements, opinions and data contained in all publications are solely those of the individual author(s) and contributor(s) and not of MDPI and/or the editor(s). MDPI and/or the editor(s) disclaim responsibility for any injury to people or property resulting from any ideas, methods, instructions or products referred to in the content.